Supporting Information

Mechanistic Basis for Red Light Switching of Azonium Ions.

Miroslav Medveď[1,2‡], Mariangela Di Donato[3,4‡], Wybren Jan Buma[5,6], Adèle D. Laurent,[7] Lucien Lameijer[8,9], Tomáš Hrivnák[2,10], Ivan Romanov,[5] Susannah Tran[11], Ben L. Feringa[8], Wiktor Szymanski[8,9],* G. Andrew Woolley[11]*

[1] Regional Centre of Advanced Technologies and Materials, Czech Advanced Technology and Research Institute (CATRIN), Šlechtitelů 241/27, 783 71, Olomouc, Palacký University Olomouc, Czech Republic
[2] Department of Chemistry, Faculty of Natural Sciences, Matej Bel University, Tajovského 40, 974 01 Banská Bystrica, Slovak Republic
[3] LENS, European Laboratory for Non-Linear Spectroscopy, via N. Carrara 1, 50019 Sesto Fiorentino (FI), Italy
[4] CNR-ICCOM, via Madonna del Piano 10, 50019 Sesto Fiorentino (FI), Italy
[5] Van 't Hoff Institute for Molecular Sciences, University of Amsterdam, Science Park 904, 1098 XH Amsterdam, The Netherlands.
[6] Institute for Molecules and Materials, FELIX Laboratory, Radboud University, Toernooiveld 7c, 6525 ED Nijmegen, The Netherlands.
[7] Nantes Université, CNRS, CEISAM, UMR 6230, F-44000 Nantes, France.
[8] Stratingh Institute for Chemistry, University of Groningen, Nijenborgh 4, 9747AF Groningen (The Netherlands)
[9] Medical Imaging Center, University Medical Center Groningen, University of Groningen Hanzeplein 1, 9713GZ Groningen (The Netherlands)
[10] Polymer Institute, Slovak Academy of Sciences, Dúbravská cesta 9, 845 41 Bratislava, Slovak Republic
[11] Dept. of Chemistry, University of Toronto, 80 St. George St., Toronto M5S 3H6 Canada
[‡] These authors contributed equally.

Table of Contents

S1. Synthesis

Starting materials, reagents and solvents were purchased from Sigma–Aldrich, Acros, Fluka, Fischer, TCI or Combi-Blocks and were used as received, unless stated otherwise. Solvents for the reactions were of quality puriss., p.a. For aqueous solutions, deionized water was used. Drying of solutions was performed with $MgSO_4$ and volatiles were removed with a rotary evaporator (Büchi, R-300). The reaction progress was monitored by TLC. All solvents and reagents were degassed using freeze-pump-thaw (3×) cycles.

Nuclear magnetic resonance spectra were measured with an Agilent Technologies 400-MR (400/54 Premium Shielded) spectrometer (400 MHz). All spectra were measured at room temperature (22–24 °C). Chemical shifts for the specific NMR spectra were reported relative to the residual solvent peak. The multiplicities of the signals are denoted by s (singlet), d (doublet), t (triplet), q (quartet), m (multiplet), br (broad signal). High-resolution mass spectrometric measurements were performed using a Thermo scientific LTQ OrbitrapXL spectrometer with ESI ionization.

Synthesis of 1,2-bis(2,6-dimethoxy-4-(piperidin-1-yl)phenyl)diazene:

To an oven-dried pressure tube, cooled under nitrogen gas, was added 1,2-bis(4-bromo-2,6-dimethoxyphenyl)diazene (30.1 mg, 65 µmol) [1], piperidine (200 µL, 1.81 mmol), $Pd_2(dba)_3$ (4.2 mg, 4.6 µmol), Cs_2CO_3 (66 mg, 0.19 mmol), RuPhos (6.1 mg, 13 µmol), and DMF (4 mL).[2] After flushing with nitrogen gas, the tube was capped with a Teflon stopper and heated in a silicone oil bath for 2 h at 110 °C and then overnight at 40 °C. The reaction was cooled to room temperature and extracted with ethyl acetate. The combined organic layers were washed with brine, dried over anhydrous Na_2SO_4, and concentrated under vacuum. The crude product was dissolved in water/MeCN mixture (1:1, v/v, final concentration 5 mg/mL) for preparative HPLC purification using a Kinetex EVO C18 column (5 µm, 100 Å, 250 x 10.0 mm) with UV detection at 365 nm. A representative chromatogram is shown below, with the collected fractions indicated:

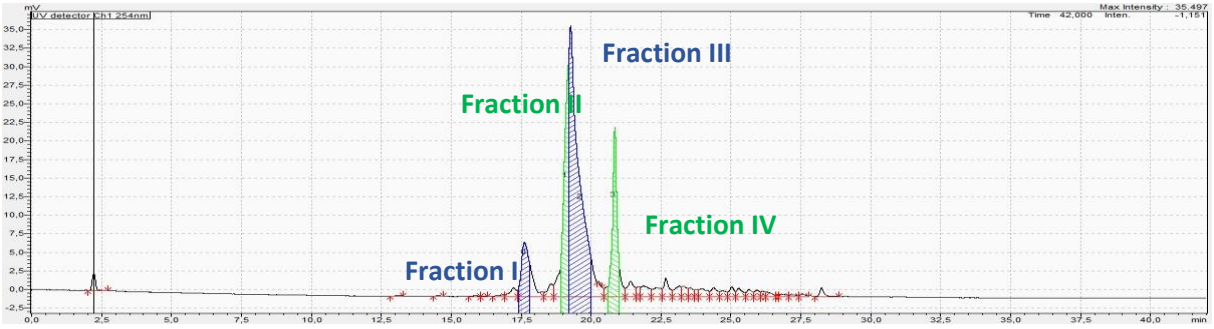

S2. Purification and identification of the product:

UPLC measurements were performed using the following setup: Column: ACQUITY UPLC® HSS T3 1.8µm, 2.1 x 150 mm; Detection: λ = 254 nm; Flow: 0.3 mL/min; Eluent A: 0.1% formic acid in water; Eluent B: 0.1% formic acid in acetonitrile; Program: (0-1 min) 5% B; (1-8 min) linear gradient to 90% B; (8-11 min) 90% B; (11-12 min) linear gradient to 5% B; (12-17 min) 5% B. All four fractions from preparative HPLC were analysed. The figure below presents the respective chromatograms, with the MS spectrum of the main HPLC peak indicated to the right of the chromatogram.

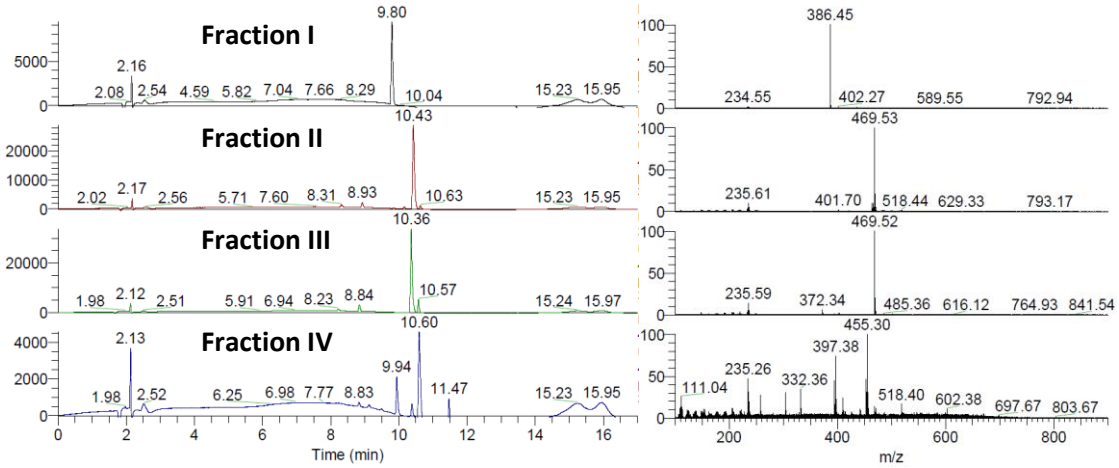

Fraction I contained the dehalogenation product derived from the mono-substituted azobenzene:

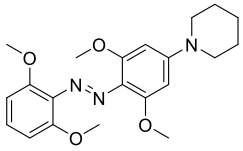

Exact Mass: 385.2002

Fractions II and III, containing the product, were collected, and subjected to lyophilization.

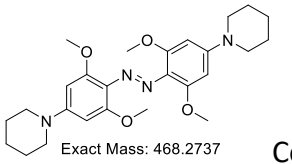

Exact Mass: 468.2737

Compound **1**

Samples for lyophilization were frozen in liquid nitrogen and then lyophilized using LaboGene CoolSafe Pro 110-4 equipment with a drum manifold and Vacuubrand RC6 chemistry hybrid pump. Conditions: temperature < -100 C, pressure < 0.01 bar, overnight. The product was isolated in the form of a free base as an orange solid. The NMR spectrum of the neutral form was obtained by dissolving a sample in CD_3OD and passing the solution through K_2CO_3.

^{1}H NMR (400 MHz, CD_3OD) δ 1.28-1.72 (m, 20H), 3.80 (s, 12H), 6.26 (s, 4H); HRMS (ESI+), calc for [M+H^{+}] ($C_{26}H_{37}N_4O_4$): 469.2809, measured: 469.2808.

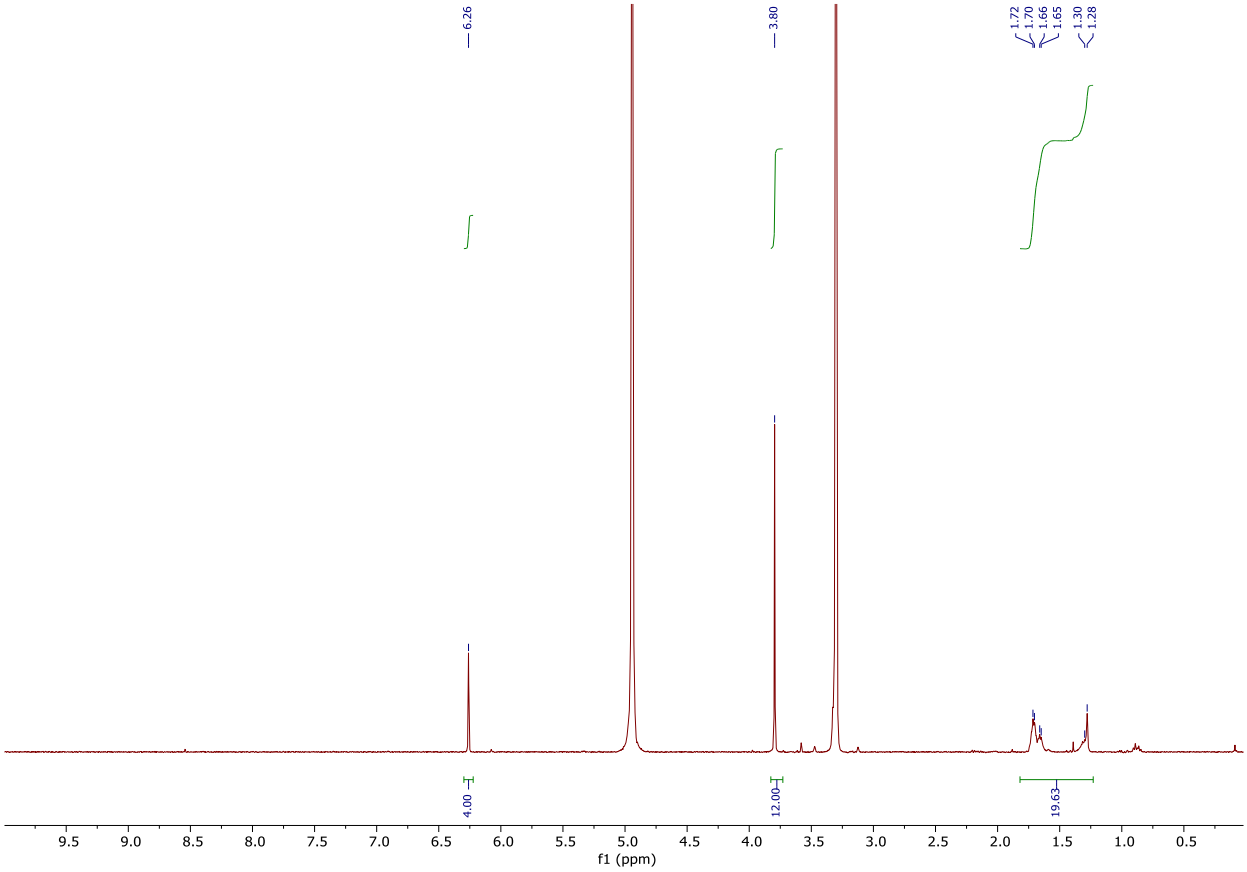

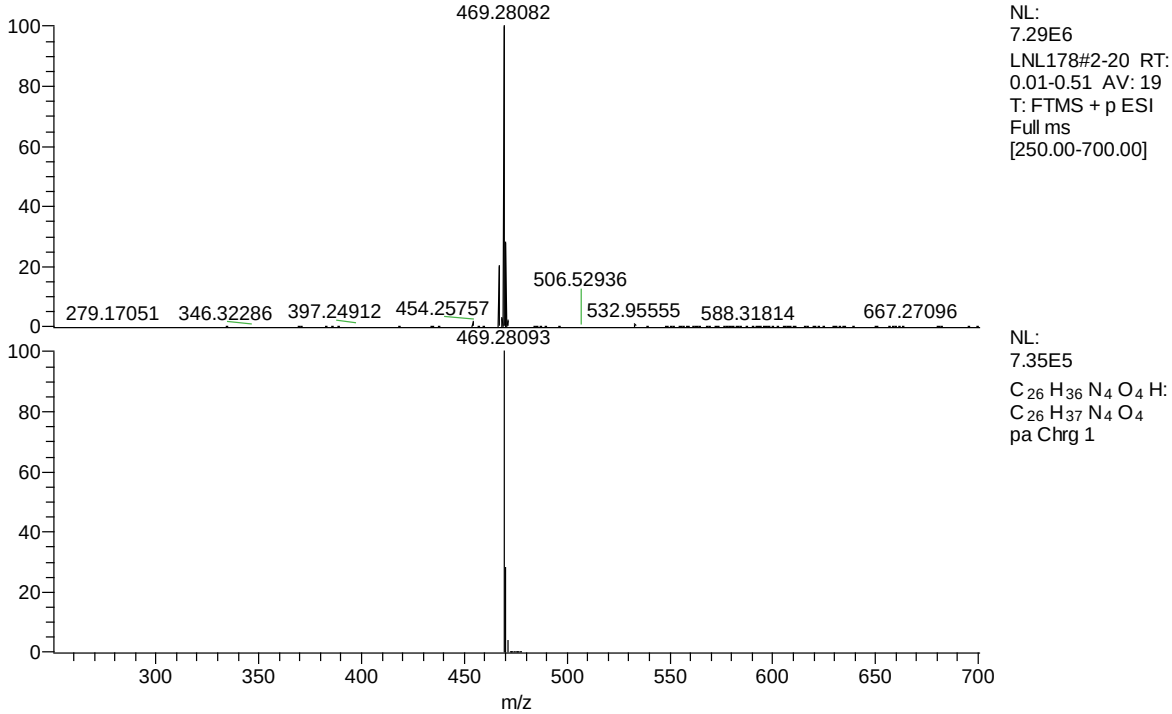

S3. UV-Vis absorbance and titration data

Absorption spectra were collected on a SPECTROstar Nano microplate reader (BMG LABTECH) or a diode array UV–Vis spectrophotometer (Ocean Optics Inc., USB4000) using 10 mm quartz cuvettes (Hellma Analytics). A stock solution of compound **1** in methanol was added to universal buffer (5 mM sodium acetate, 5 mM tris(hydroxymethyl)aminomethane, 5 mM 2-(*N*-morpholino)ethane sulfonic acid, 5 mM 3-(cyclohexylamino)-2-hydroxy-1-propane sulfonic acid) and the pH was measured directly. SVD analysis to produce spectra in Fig. 1a was performed using Kintek Explorer as described.[3]

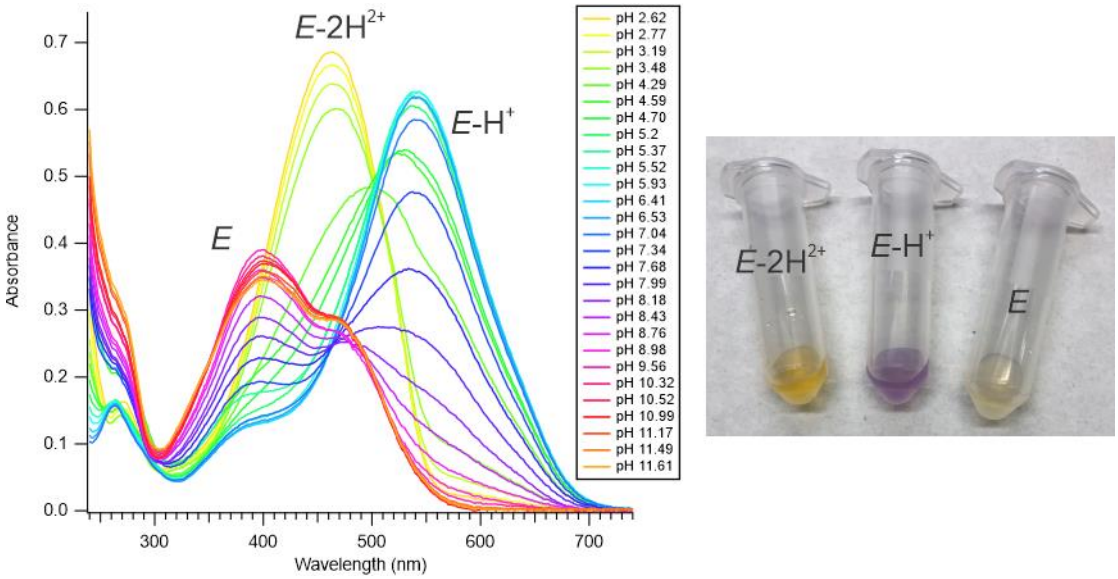

Fig. S3.1. UV-Vis titration of compound **1**.

S4. Steady state photoswitching data

Solutions of compound **1** were irradiated from the side in a fluorescence quartz cuvette (optical path = 1 cm), using either a custom-built (Prizmatix/Mountain Photonics) or Thorlabs multi-wavelength fiber coupled LED-system. The LEDs were controlled automatically via the built-in USB-controller using FC-LED-Ctrl 3.0 and MacroCreator 5.05 or a Mightex control system. Power measurements were carried out using a Thorlabs PM160T directly after the cell holder. Temperature was maintained using a Quantum Northwest TC1 temperature controller. Electronic absorption spectra were measured using an Agilent 8453 or Ocean Optics diode array spectrophotometers.

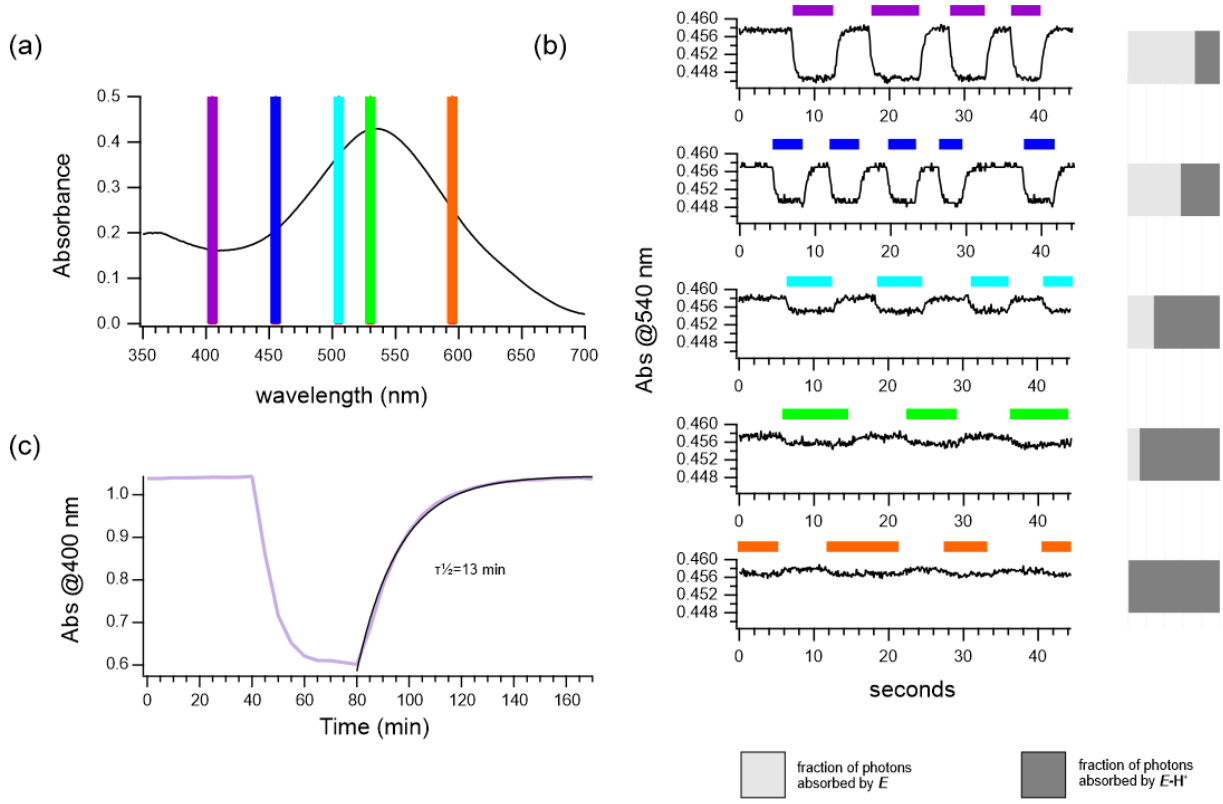

Fig. S4.1. Steady state photoswitching of compound **1**.

(a) A solution of **1** in potassium phosphate buffer, pH 7.4, 2 °C, was irradiated with LEDs with wavelengths shown (405 nm, 455 nm, 505 nm, 530 nm, 595 nm). LED intensities were adjusted so that total number of photons absorbed per second was the same at each wavelength (1.1×10^{16} photons/s). (b) Absorbance changes at 540 nm versus time upon irradiation with the wavelengths shown. The fraction of the total photons absorbed per second, absorbed by ***E*** and ***E*-H$^+$** is shown. As the fraction absorbed by ***E*-H$^+$** increases, smaller changes are seen in the absorbance indicating that the quantum yield for photoswitching from ***E*-H$^+$** to ***Z*-H$^+$** is smaller than that for switching from ***E*** to ***Z***. (c) Photoswitching and thermal relaxation of the ***E*** form at pH 11.6 at 20°C. A half-life of 13 min corresponds to a rate constant of 0.001 s^{-1}.

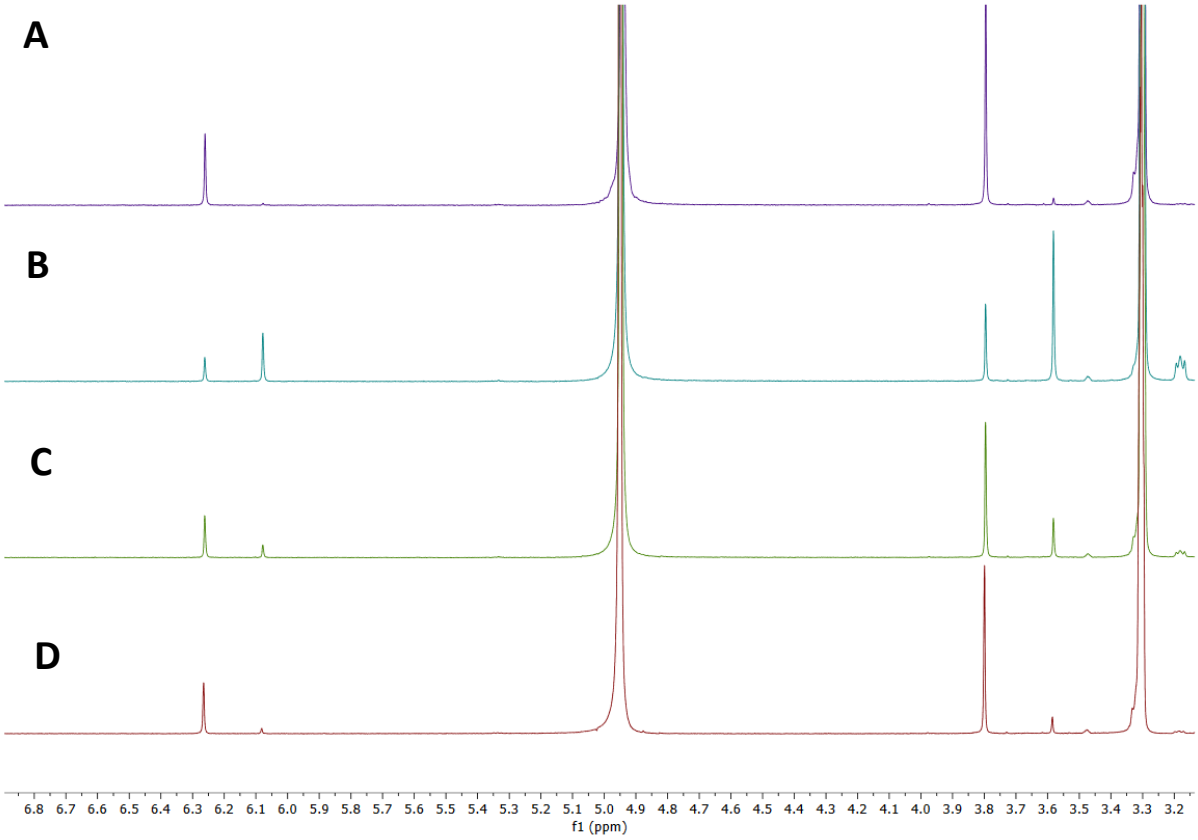

Fig. S4.2. NMR analysis photoswitching and thermal relaxation of compound **1** in methanol.

To a solution of compound **1** in methanol-d_4, 100 mg of potassium carbonate was added. The solution was passed through a cotton plug to separate the salts and recover the compound in the neutral form dissolved in methanol-d_4 (approx. 50:1 ***E***/***Z***)(**A**). Sample (**A**) was then irradiated for 1 min at λ = 430 nm, leading to the sample (**B**) enriched in the ***Z***-isomer (approx. 1:2 ***E***/***Z***). Sample **B** was then stored at room temperature in the dark for three days, leading to the distribution presented in spectrum **C** (approx. 3:1 ***E***/***Z***). Short heating of sample **C** led to sample **D**, with almost full recovery of the initial spectrum. These data indicate that the thermal ***Z***-***E*** switching is a clean process that proceeds with >1 day half-life in methanol.

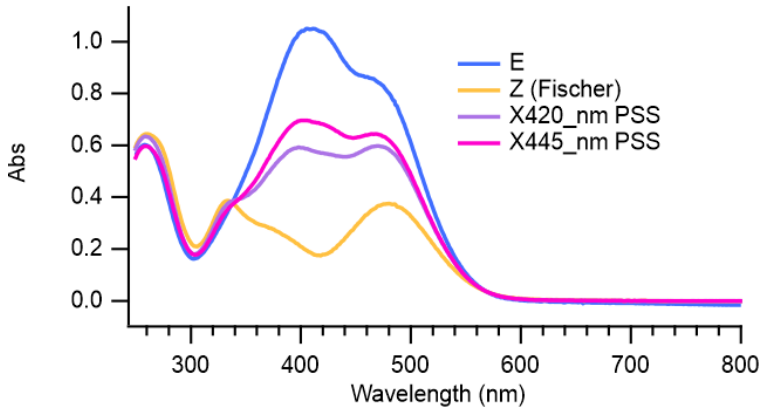

Fig. S4.3. Spectrum of the *Z* form in methanol using the method of Fischer.

A solution of **1** in methanol in the dark-adapted ***E*** form, was irradiated to the photostationary state (PSS) with light of 420 nm or 445 nm. The spectrum of the *Z* form was then estimated using the method of Fischer.[4]

S5. Ultrafast transient absorption spectroscopy

The apparatus used for the transient absorption spectroscopy (TAS) measurements is based on an integrated home-made Ti:sapphire oscillator able to produce 80 fs pulses centered at 810 nm, coupled with a regenerative amplifier system (Amplitude Pulsar). The final output of the regenerative amplifier consists in 150 fs pulses centered at 785 nm with an average power of 450-500 mW at 1 kHz repetition rate. Visible pump pulses were generated by pumping a home-made non-collinear optical parametric amplifier (NOPA) with a portion of the fundamental 785 nm radiation. The pump beam polarization was set to magic angle with respect to the probe beam by rotating a $\lambda/2$ plate, to exclude rotational contributions. The excitation wavelength was set at 530 nm and excitation power was set at 50 nJ for all measurements. The white light probe pulses were generated by focusing a small portion of the fundamental laser radiation on a 3 mm thick CaF_2 window, kept under continuous rotation to avoid damage. The generated white light was divided in two portions through a 50/50 beam splitter as to obtain a reference and probe beam. The probe beam was focused at the sample position using a 75 mm spherical mirror and overlapped with the pump beam, while the reference crossed the sample in a different position. After passing through the sample the white light probe and reference pulses were both directed to a flat field monochromator coupled to a home-made CCD detector. Transient signals were acquired in a time interval spanning up to 100 ps. The sample was contained in a 2 mm quartz cuvette, mounted on a movable holder to minimize photodegradation. Measurements were performed at room temperature. Concentrations were adjusted to an absorbance of 0.9 – 1.0 OD (for the respective optical path) at the absorption maximum which amounted to about 0.3 – 0.5 OD at excitation wavelength. Before and after the measurements, the integrity of the sample was checked on a PerkinElmer LAMBDA 950 spectrophotometer.

Transient data were analyzed using a global analysis procedure[5] and applying a linear decaying kinetic scheme using the software Glotaran.[6] Before global analysis data were subjected to Singular Value Decomposition (SVD)[7] to identify the number of significant decay constants.

S6. Nanosecond transient absorption spectroscopy

Nanosecond transient absorption spectra were recorded with an in-house assembled setup. Excitation was performed using a tunable Nd:YAG-laser system (NT342B, Ekspla) comprising a pump laser (NL300) with harmonics generators (SHG, THG) producing 355 nm to pump an optical parametric oscillator (OPO) with SHG connected in a single device. This laser system was operated at a repetition rate appropriate for the recovery time of the investigated sample, that is, at least lower than the inverse of five times the observed recovery time, and with a maximum repetition rate of 5 Hz. The probe light was generated by a high-stability short arc xenon flash lamp (FX-1160, Excelitas Technologies) using a modified PS302 controller (EG&G). This flash lamp was either operated at double the repetition rate of the excitation laser, or in bursts of shots separated by 40 ms and with a delay ranging from 0 to 39 ms with respect to the excitation laser pulse for laser repetition rates lower than 2 Hz. Using a 50/50 beam splitter, the probe light was split equally into a signal beam and a reference beam and focused on the entrance slit of a spectrograph (SpectraPro-150, Princeton Instruments). The probe beam ($A = 1\ mm^2$) was passed through the sample cell and orthogonally overlapped with the excitation beam on a 1 mm × 1 cm area. The excitation energy was recorded by measuring the excitation power at the back of an empty sample holder. To correct for fluctuations in the flash lamp spectral intensity, the reference was used to normalize the signal. Both beams were

recorded simultaneously using a gated intensified CCD camera (PI-MAX3, Princeton Instruments) which has an adjustable gate of minimal 2.9 ns. A delay generator (DG535, Stanford Research Systems, Inc.) was used to time the excitation pulse, the flash lamp, and the gate of the camera. The setup was controlled by an in-house written LabView program. Transient absorption spectra were analyzed similarly to the fs transient absorption data, that is, using the global analysis implemented in the Glotaran[6] software after identification of the number of significant decay constants using Singular Value Decomposition (SVD).[7]

Figure S6.1 shows the transient absorption data of compound **1** in solutions at different pH values obtained with ns excitation at 535 nm at 20 ± 0.5ºC, as well as the EADS resulting from a global analysis of these data. The lifetimes of the two components are collected in Table S6.1. Analogous data obtained at pH 6.9 and pH 8.8 are given in the main text. Note the logarithmic time scale.

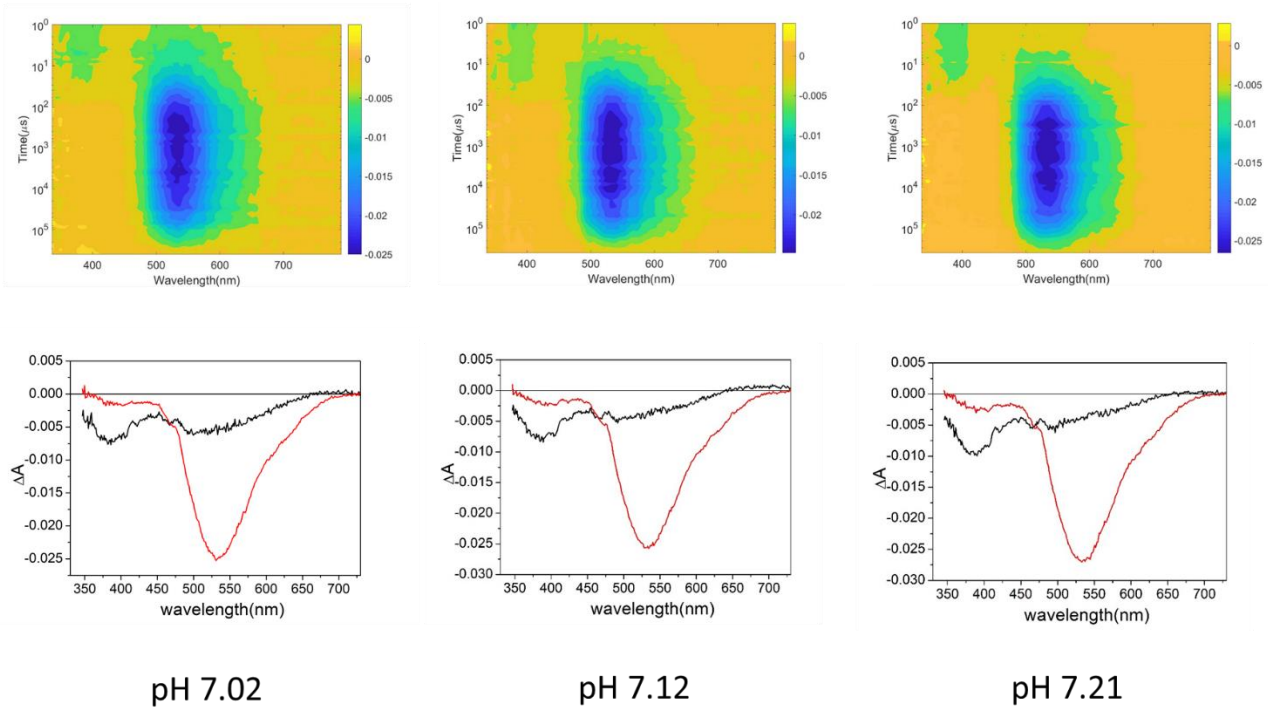

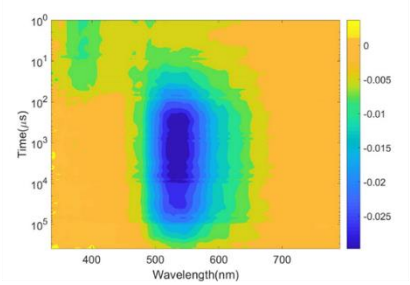

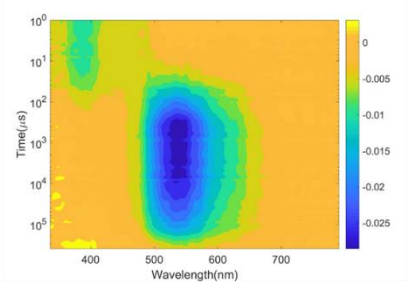

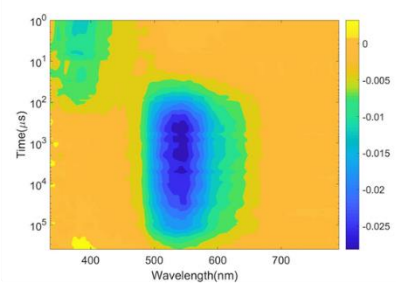

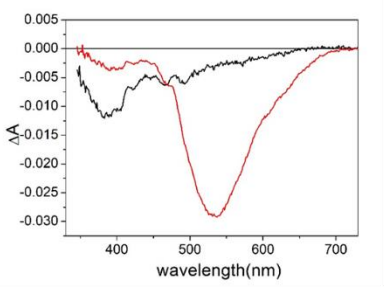

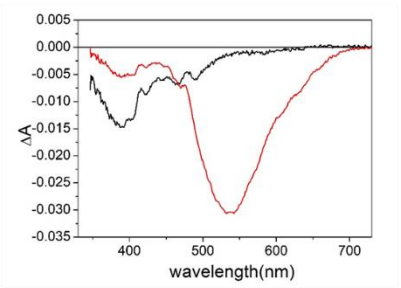

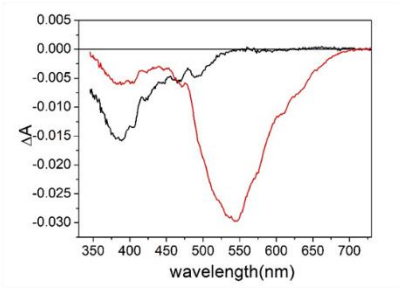

pH 7.31 pH 7.42 pH 7.51

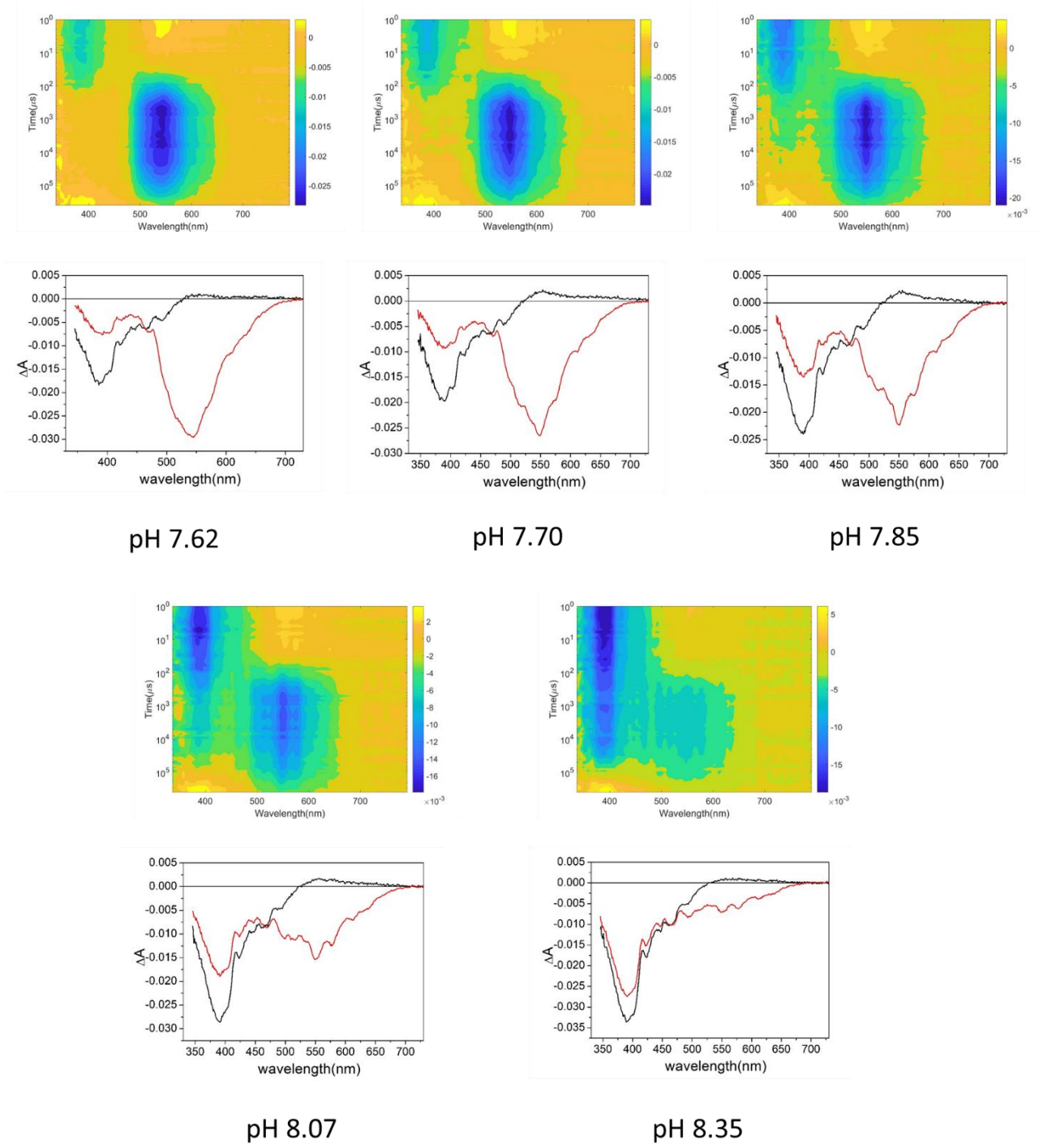

Figure S6.1. Nanosecond transient absorption data with excitation at 535 nm.

Heat maps of nanosecond transient absorption data of compound **1** obtained with excitation at 535 nm with pulse energies of about 2.3 mJ (top) and their global analyses (bottom) for solutions at different pH values at 20 ± 0.5ºC.

To investigate the proposed restoration of acid-base equilibria between ***E***, ***Z***, ***E*-H$^+$**, and ***Z*-H$^+$** as underlying the observed changes in the ns transient absorption spectra, we also obtained such spectra for excitation at 400 nm. At this wavelength, we predominantly excite ***E***. Figure S6.2 shows transient absorption data at different pH values obtained with ns excitation at 400 nm, as well as the EADS resulting from a global analysis of these data. The lifetimes of the two components are collected in Table S6.1. As with irradiation at 535 nm, these transient absorbance measurements have a repetition rate of ~ 1 Hz. Therefore, whenever a relaxation time becomes longer than about 200 ms, recovery is incomplete, and a signal remains (as we also commented upon for 535 nm excitation). The τ_1 values at 400 nm are therefore reliable but the τ_2 values much less so.

Excitation at 400 nm will, in the first instance, photoisomerize part of ***E*** into ***Z***. We thus expect a decrease of the 380 nm absorption while the 540 nm band should not be affected, as is indeed confirmed by the black EADS in Figure S6.2 which show a bleach at 380 nm and minor changes at 540 nm that decrease for higher pH values. Subsequently, the acid-base equilibria are re-established during which part of the ***E*-H$^+$** population will deprotonate to form ***E***, which has been *depleted* in the photoisomerization step while part of the population of ***Z*** that has been *formed* in the photoisomerization step will be protonated to form ***Z*-H$^+$**depending on the pH. These changes will manifest themselves in the transient absorption spectra by a recovery of the 380 nm band, and an increase of the bleach at 540 nm because of the drop in ***E*-H$^+$** population which cannot be compensated by the amount of ***Z*-H$^+$** that is produced in re-establishing the ***Z*** $\leftrightarrow$ ***Z*-H$^+$** equilibrium. This is indeed observed when comparing the black and red EADS. We thus conclude that the 400 nm spectra confirm the conclusions that have been drawn from the 530 nm spectra.

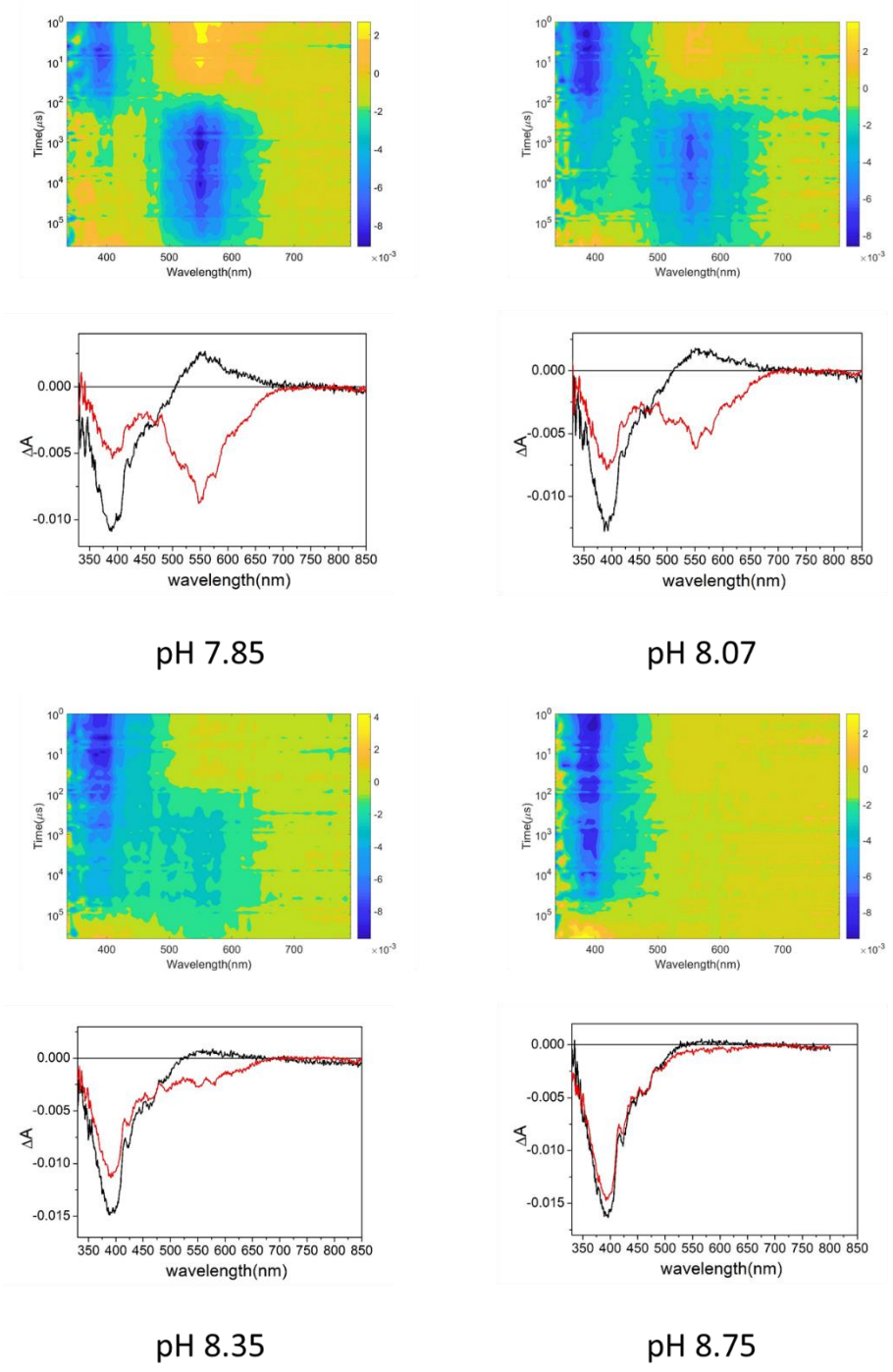

Figure S6.2. Nanosecond transient absorption data with excitation at 400 nm.

Heat maps of nanosecond transient absorption data of compound **1** obtained with excitation at 400 nm with pulse energies of about 0.3 mJ (top) and their global analyses (bottom) for solutions at different pH values.

pH	τ_1 (µs)[a]	τ_2 (ms)[a]	τ_1 (µs)[b]	τ_2 (ms)[b]
6.85	41	129		
7.02	44	134		
7.12	46	172		
7.21	64	193		
7.31	77	202		
7.42	86	234		
7.51	93	243		
7.62	117	252		
7.7	131	260		
7.85	130	259	141	436
8.07	143	267	146	313
8.35	147	223	158	108
8.75	199	256	114	244

[a]530 nm excitation; [b]400 nm excitation

Table S6.1. Lifetimes resulting from the analyses of the transient absorption data.
Data shown in Figures S6.1. (excitation at 535 nm) and S6.2. (excitation at 400 nm) were analyzed and gave rise to the black and red EADS lifetimes τ_1 and τ_2, respectively.

S7. Theoretical considerations and computational methods.

The ground state (GS) structures of the ***E***, ***E*-H$^+$**, ***E*-2H^{2+}**, ***Z*** and ***Z*-H$^+$** forms of compound **1** were optimized using the M06-2X functional[8] in combination with the 6-31+G(d) atomic basis set.[9] This exchange-correlation functional is known to perform well not only for the GS thermochemistry, but also in describing excited states. The *ultrafine* integration grid, tight self-consistent field and geometry optimization were applied to all computations starting from various chemically plausible conformers. All minima were checked for the presence of imaginary frequencies by performing the vibrational frequency analysis. The appropriateness of the applied level of theory was checked against the domain-based local pair natural orbital (DLPNO)[10] coupled cluster with singles and doubles and perturbative triples (CCSD(T))[11-12] single-point calculations applying the TightPNO settings as defined in Liakos et al.[13] with the cc-pVTZ basis[14] were performed using the geometries obtained with DFT. The solvent effects were considered employing the implicit Solvation Model based on Density (SMD).[15] As the implicit solvent models are not capable of capturing specific solute-solvent interactions such as hydrogen bonds and structural peculiarities of the solvation shell, the explicit solvation approach was also applied to describe the aqueous environment (see Section S11). The pK_a values of ***E*-H$^+$** and ***Z*-H$^+$** forms were estimated using the protocol proposed by Lian et al.[16] To determine the activation barriers for the thermal back-isomerization of ***E*-H$^+$** to ***Z*-H$^+$** and ***E*** to ***Z***, relaxed scans for GS torsional rotation and N-inversion pathways were first performed, followed by full transition state (TS) optimizations at the U-M06-2X/6-31+G(d)/SMD level. Again, the true nature of the TSs (corresponding to first-order saddle points with a single imaginary frequency) was confirmed by vibrational frequency analysis. The adequateness of the single-reference density functional theory (DFT) approach in the TS region was checked by performing spin-flip time-dependent (SF-TD)-DFT calculations at the BHHLYP/6-31++G(d,p)/SMD level for the key GS structures. SF-TD-DFT is an extension of DFT to situations when the consideration of non-dynamical correlation effects is relevant, i.e., it is also suitable for semi-quantitative analysis of systems in the vicinity of a conical intersection. The method is based on the spin-flip approach which is suitable for describing multireference wave functions within a single reference formalism as spin–flipping, e.g., α→β, excitations from a high-spin (M_s=1) triplet reference state.[17-18]

The theoretical absorption spectra of the ***E***, ***E*-H$^+$**, ***E*-2H^{2+}**, ***Z*** and ***Z*-H$^+$** forms of compound **1** were obtained by computing the vertical excitation energies (VEEs) and oscillator strengths (*f*) for three lower singlet excited states (ES). The inhomogeneous broadening of spectral lines was accounted for by applying the full-width-at-half-maximum (FWHM) parameter of 0.8 eV. First, the gas-phase spectra were acquired by the time-dependent M06-2X and CAM-B3LYP functionals[19] as well as the second-order coupled-cluster (CC2)[20] wavefunction-based methods in combination with the 6-31++G(2df,2p) and def2-TZVPP basis sets, respectively. The CAM-B3LYP functional showed better agreement with CC2 than M06-2X for the investigated systems. Therefore, to account for the solvent effects on electronic transitions, the CC2 gas-phase VEEs and *f* values were corrected by using CAM-B3LYP in combination with the SMD model employing the linear-response (LR), corrected linear response (cLR)[21] as well as LR-cLR (also referred to as cLR^2)[22] approaches within the non-equilibrium regime. The latter approach includes the dynamical response of the solvent to the solute transition density (so-called ES dispersion contribution captured by LR) as well as a perturbative correction of the state-specific polarization of the solvent due to the ES density (cLR) and was shown to be superior to both LR and cLR for various types of transitions.[22] The performance of the 6-31++G(2df,2p) double-zeta basis set in evaluating VEEs was shown to

be comparable to its triple-zeta analog (6-311++G(2df,2p)). ES (S_1) optimizations and the ES relaxed scans along the ESIPT and isomerization pathways were carried out at the TD-M06-2X/6-31+G(d)/SMD level under the equilibrium solvation regime. The SF-TD-BHHLYP/6-31++G(d,p) approach was applied to check the adequateness of TD-DFT in the region close to the conical intersection point (CI) as well as to optimize the minimum energy CI structures (in the gas phase). All (TD-)DFT calculations were performed using the Gaussian09[23] and Gaussian16.[24] The SF-TD-DFT and CC2 computations were carried out with Gamess[25-26] and Turbomole respectively.[27]

To model the aqueous environment explicitly, molecular dynamics (MD) simulations were performed using the Amber14 program suite.[28-30] An initial 0.2 ns equilibration run was done using the GAFF[31] and SPC-Fw[32] classical force-fields, with the former used to describe the solute and the latter for the representation of 3000 water molecules as well as Cl^- counterions (a cubic box of 4.5 nm). During this initial equilibration, the solute geometries were kept frozen at their M06-2X/6-31+G(d)/SMD optimized geometries, with partial charges calculated at the M06-2X/6-311++G(2df,2p) level using the CHELPG procedure[33] as implemented in Gaussian16 program. After this step, two different types of quantum-mechanics/molecular-mechanics (QM/MM) simulations were performed. First, we used the DFTB3 approach[34-36] as implemented in Amber14 to describe the solute molecule, applying the DFTB3/3OB parameter set as defined by Gaus et al..[36] The whole system was further equilibrated at the DFTB/SPC-Fw level for 0.2 ns. From the subsequent 1 ns production run, 50 equally time-separated snapshots were sampled and used for QM VEE calculations. In the second approach, used only for the *E* form, we carried out *ab-initio* QM/MM MD simulations using Amber14/Gaussian09 interface, with the solute described at the M06-2X/6-31G(d) level of theory. To increase the sampling efficiency, we followed a "branching" approach, with a shorter 1 ps M06-2X/6-31G(d)/SPC-Fw production runs starting from 25 equally time-separated points of the 1 ns classical MD (GAFF/SPC-Fw) simulation, in which the solute geometry remained frozen. For the M06-2X/6-31G(d)/SPC-Fw simulations, two snapshots were sampled at the 0.5 ps and 1.0 ps time points from each trajectory. For the GAFF/SPC-Fw and DFTB/SPC-Fw simulations, an NPT ensemble was used with the time step of 1 fs, pressure was kept at 1 atm using the Berendsen barostat, and the non-bonding MM and QM/MM interaction cut-off ranges were set to 9 Å and 7 Å, respectively. In the case of M06-2X/6-31G(d)/SPC-Fw simulations, a non-periodic ensemble was employed, the time step was reduced to 0.5 fs, a SHAKE algorithm[37] was used for hydrogen atoms of the solute, and the MM and QM/MM cut-off ranges were set to the values large enough to include all possible intermolecular interactions (i.e., 9999 Å). All MD simulations were done at 300 K using the Langevin dynamics with collision frequency of 5 ps^{-1}.

The effect of explicit solvation on excitation energies was considered using the polarizable embedding (PE) approach,[38-39] as implemented in Dalton2019[40] (Dalton, a molecular electronic structure program, Release Dalton2019.alpha (2019), see http://daltonprogram.org). All PE calculations were done using the CAM-B3LYP functional in combination with the smaller 6-311+G(d) basis set to avoid any potential electron spill-out effects.[41] The final electronic spectra obtained from the PE solvation model were constructed from the snapshot-averaged histograms computed at 20 nm intervals, starting from 200 nm up to 800 nm, as a sum of oscillator strengths of the first three excitations.

Distributed multipoles, up to quadrupoles, and anisotropic polarizabilities were computed using the LoProp procedure[42] as implemented in the OpenMolcas program[43] at the B3LYP/aug-cc-pVTZ level. This distribution scheme and the level of theory was shown to perform well in description of the electrostatic potential due to the permanent multipole and

induced dipole moments of water molecules.[38, 44] The reference atom-localized properties were rotated to molecule-specific spatial orientation using an in-house program.

S8. Ground state structures of *E*-H$^+$, *Z*-H$^+$, *E*, *Z*, and corresponding TS

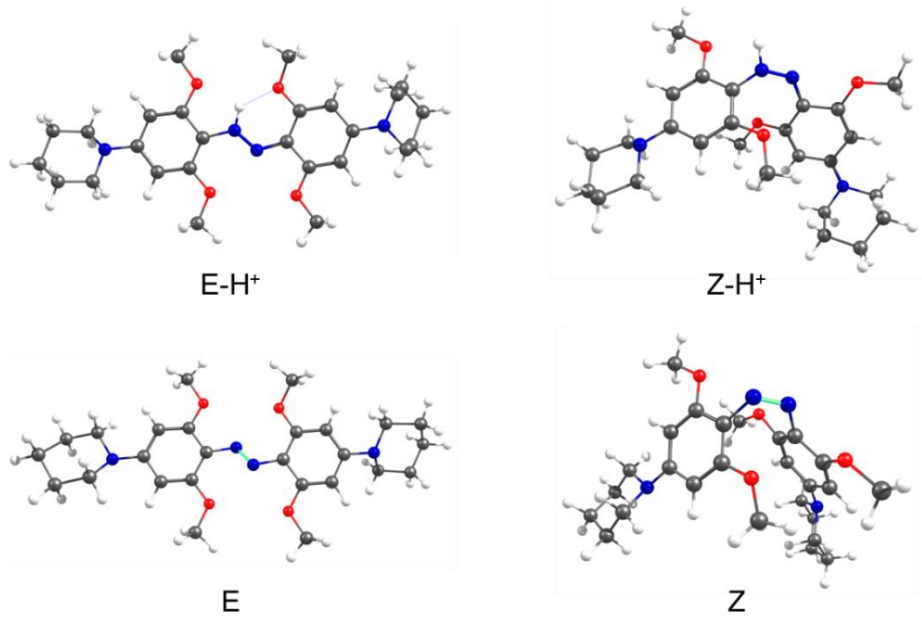

Figure S8.1. Ground state structures of *E*-H$^+$, *Z*-H$^+$, *E*, and *Z* forms.
Structures were optimized at the M06-2X/6-31+G(d)/SMD (water) level.

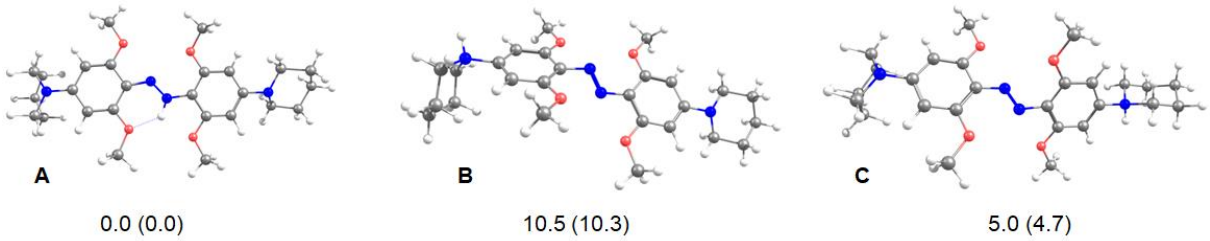

Figure S8.2. Alternative protonation sites are less favored.
Structures of the mono-protonated ***E***-form (***E*-H**$^+$) optimized at the M06-2X/6-31+G(d)/SMD (water) level of theory with the proton added to the piperidine unit (B,C) rather than the azo unit. Relative electronic energies and standard Gibbs energies (T = 298.15 K) (given in parentheses) with respect to the most stable isomer are given in kcal/mol.

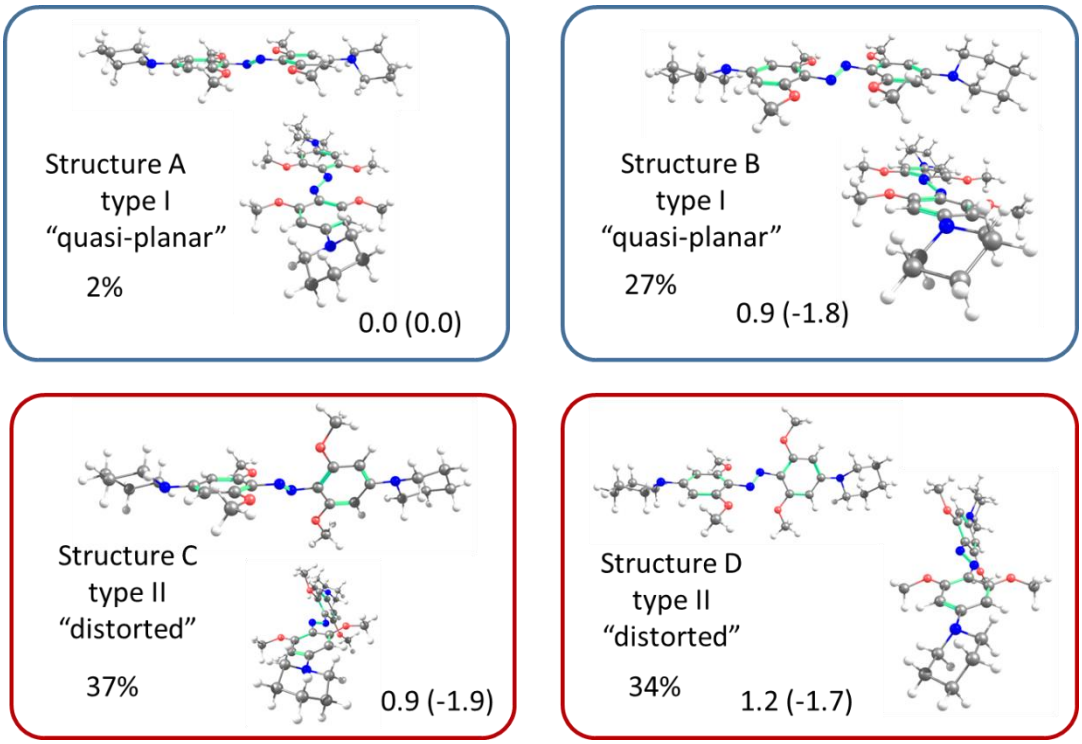

Figure S8.3. Alternative ground state structures of the ***E*** form

Optimized structures and relative electronic energies (standard Gibbs energies, T = 298.15 K, in parentheses) of quasi-planar (type I) and distorted (type II) conformers of the ***E*** form computed at the M06-2X/6-31+G(d)/SMD (water) level. All values are given in kcal/mol. The Boltzmann distribution of conformers was calculated based on standard Gibbs energy values (T = 298.15 K).

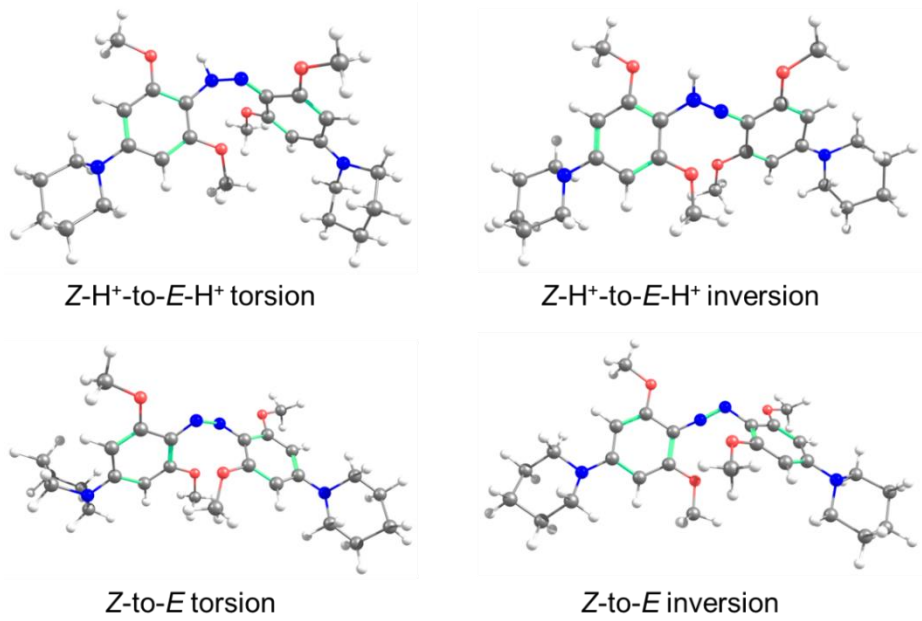

Figure S8.4. Transition state structures for thermal isomerization.

Structures optimized at the U-M06-2X/6-31+G(d)/Guess (INDO, Mix, always)/SMD (water) level.

Table S8.1. Reaction electronic and Gibbs energies and activation barriers for thermal isomerization.

Energies (kcal/mol, T = 298.15 K) of neutral and protonated species were calculated at various levels of theory using the M06-2X/6-31+G(d)/SMD (water) structures displayed in Figures S8.1-4.

Reaction energies	ΔE		$\Delta G°$	
	E(**E**) – E(**Z**)	E(**Z**-H$^+$) – E(**E**-H$^+$)	$G°$(**E**) – $G°$(**Z**)	$G°$(**Z**-H$^+$) – $G°$(**E**-H$^+$)
R-M06-2X/6-31+G(d)	0.0[a]	3.8	-0.2[a]	4.2
R-DLPNO-CCSD(T)/ cc-pVTZ	0.7[a]	4.5	0.6[a]	4.8
R-M06-2X/6-31+G(d)	0.3[b]	3.8	-1.9[b]	4.2
Thermal barriers for Z-to-E back-isomerization	E(TS) – E(**Z**)	E(TS-H$^+$) – E(**Z**-H$^+$)	$G°$(TS) – $G°$(**Z**)	$G°$(TS-H$^+$) – $G°$(**Z**-H$^+$)
TORSION U-M06-2X/6-31+G(d)/ Guess (INDO, Mix, always)	29.9	18.0	25.5	19.0
INVERSION U-M06-2X/6-31+G(d)/ Guess (INDO, Mix, always)	35.4	24.7	32.4	24.7

[a] The values obtained considering quasi-planar structure A of the ***E*** form (see Figure S8.3).
[b] The values obtained considering the Boltzmann populations of A-D conformers of the ***E*** form based on their relative standard Gibbs energies (T = 298.15 K, see Figure S8.3).

S9. Estimation of pK$_a$s

$$E\text{-H}^+ \text{ (aq)} \rightleftarrows E \text{ (aq)} + \text{H}^+ \text{ (aq)} \quad (1)$$
$$Z\text{-H}^+ \text{ (aq)} \rightleftarrows Z \text{ (aq)} + \text{H}^+ \text{ (aq)} \quad (2)$$
$$pK_a(\text{X-H}^+) = \frac{\Delta G^*_{aq}}{2.303RT} \quad (3)$$
$$\Delta G^*_{aq}(\text{X-H}^+) = G^*_{aq}(\text{H}^+) + G^*_{aq}(\text{X}) - G^*_{aq}(\text{X-H}^+) \quad (4)$$
$$G^*_{aq}(\text{H}^+) = G^o_g(\text{H}^+) + \Delta G_{aq,solv}(\text{H}^+) + \Delta G^{0\rightarrow *}(\text{H}^+) = \text{-270.3 kcal/mol} \quad (5)$$

The standard state aqueous Gibbs energy of a proton, $G^*_{aq}(\text{H}^+)$ includes the gas-phase Gibbs energy of a proton ($G^o_g(\text{H}^+)$ = −6.29 kcal/mol), the experimentally measured hydration Gibbs energy ($\Delta G_{aq,solv}(\text{H}^+)$= −265.9 kcal/mol) and $\Delta G^{0\rightarrow *}(\text{H}^+)$ is used to convert from the 1 atm ideal gas standard state to the 1 M standard state, where the superscripts ° and * indicate the 1 atm and 1 M standard states, respectively: $\Delta G^{0\rightarrow *}(\text{H}^+) = RT\ln 24.46 = 1.89$ kcal/mol at 298 K.

Table S9.1. Calculated Gibbs energies and pK$_a$s

The standard state aqueous Gibbs energies (kcal/mol) and pK$_a$ calculated by eq. (3) at the M06-2X/6-31+G(d)/SMD (water) level of theory.

Reaction	$G^*_{aq}(\text{X}) - G^*_{aq}(\text{X-H}^+)$	$\Delta G^*_{aq}(\text{X-H}^+)$	$pK_a(\text{X-H}^+)$ theor.	exp.
E-**H**$^+$ (aq) ⇄ ***E*** (aq) + **H**$^+$ (aq)	279.6	9.3	6.8[a]	7.7
Z-**H**$^+$ (aq) ⇄ ***Z*** (aq) + **H**$^+$ (aq)	277.4	7.1	5.2	5.8
Stabilization Gibbs energy/pK$_a$ change	-2.2	-2.2	-1.6	-1.9

[a] The value obtained considering distorted structure C of the E form (see Figure S8.2).

S10. Electronic transitions

Vertical excitation energies (VEEs) for the 3 lowest singlet ES of ***E*-H$^+$, *Z*-H$^+$**, ***E*** and ***Z*** were calculated in the gas phase and water using the Linear Response (LR) as well as corrected Linear Response (cLR) approach. Basis set dependence of VEE was tested. MO analysis of the electronic transitions was performed. The effect of including explicit water molecules on VEEs of chromophores was also studied (see Section S11).

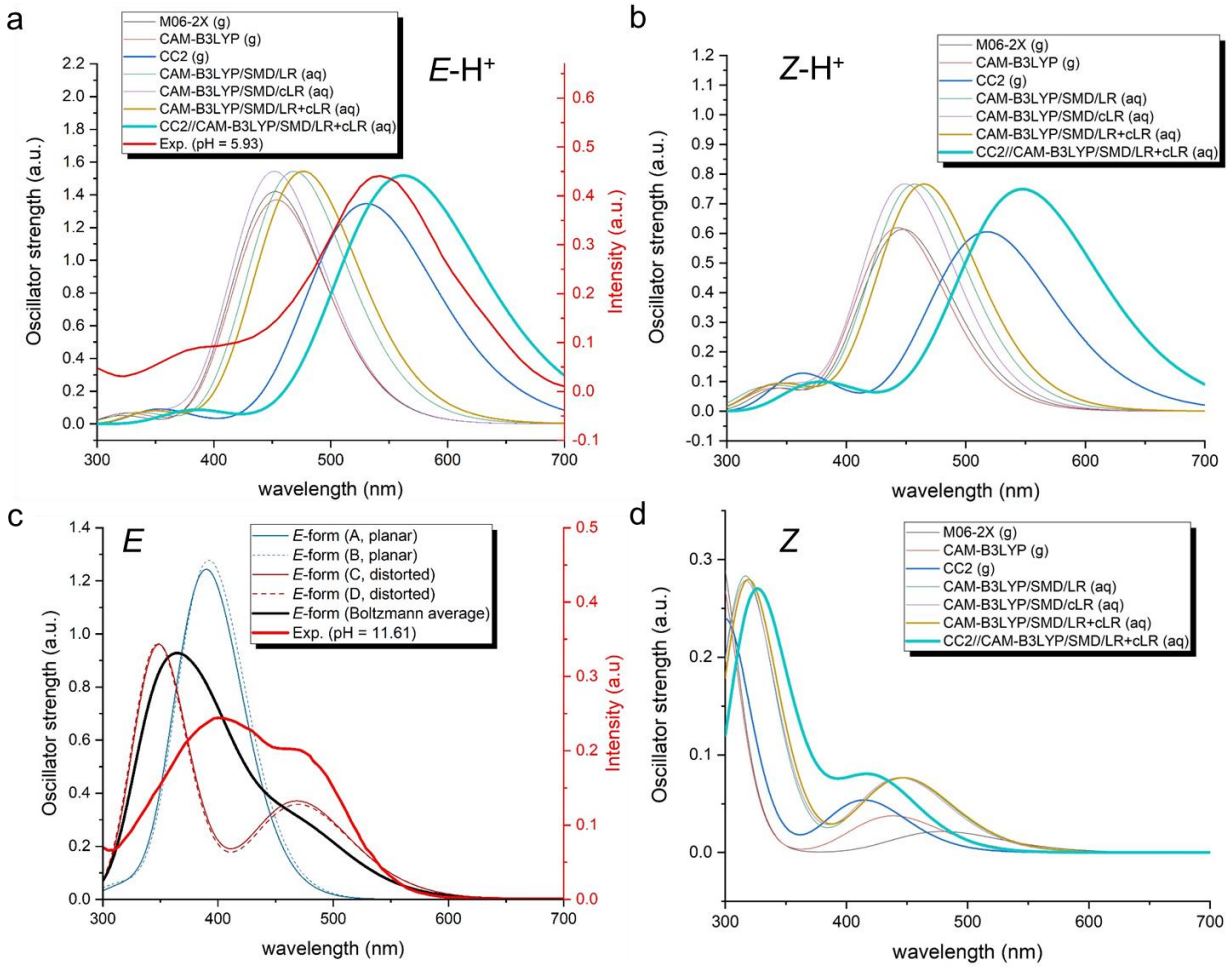

Figure S10.1. UV-Vis electronic absorption spectra of different forms of compound **1** in the gas phase and aqueous environment.

The simulated spectra (FWHM = 0.8 eV) were obtained by TD-DFT and CC2 methods using the 6-31++G(2df,2p) and def2-TZVPP basis sets, respectively, in the gas phase and by employing the LR, cLR and LR+cLR approaches combined with the SMD implicit solvation model at the CAM-B3LYP/6-31++G(2df,2p) level in the aqueous environment. The CC2//LR-cLR-CAM-B3LYP/SMD spectrum was obtained by shifting the LR-cLR-CAM-B3LYP spectrum (at the energy scale) by the difference between the gas phase CC2 and CAM-B3LYP spectra. In the case of the *E* form (panel c), the theoretical spectra were obtained using the composite CC2//LR-cLR-CAM-B3LYP/SMD approach based on data displayed in Figure S10.2.

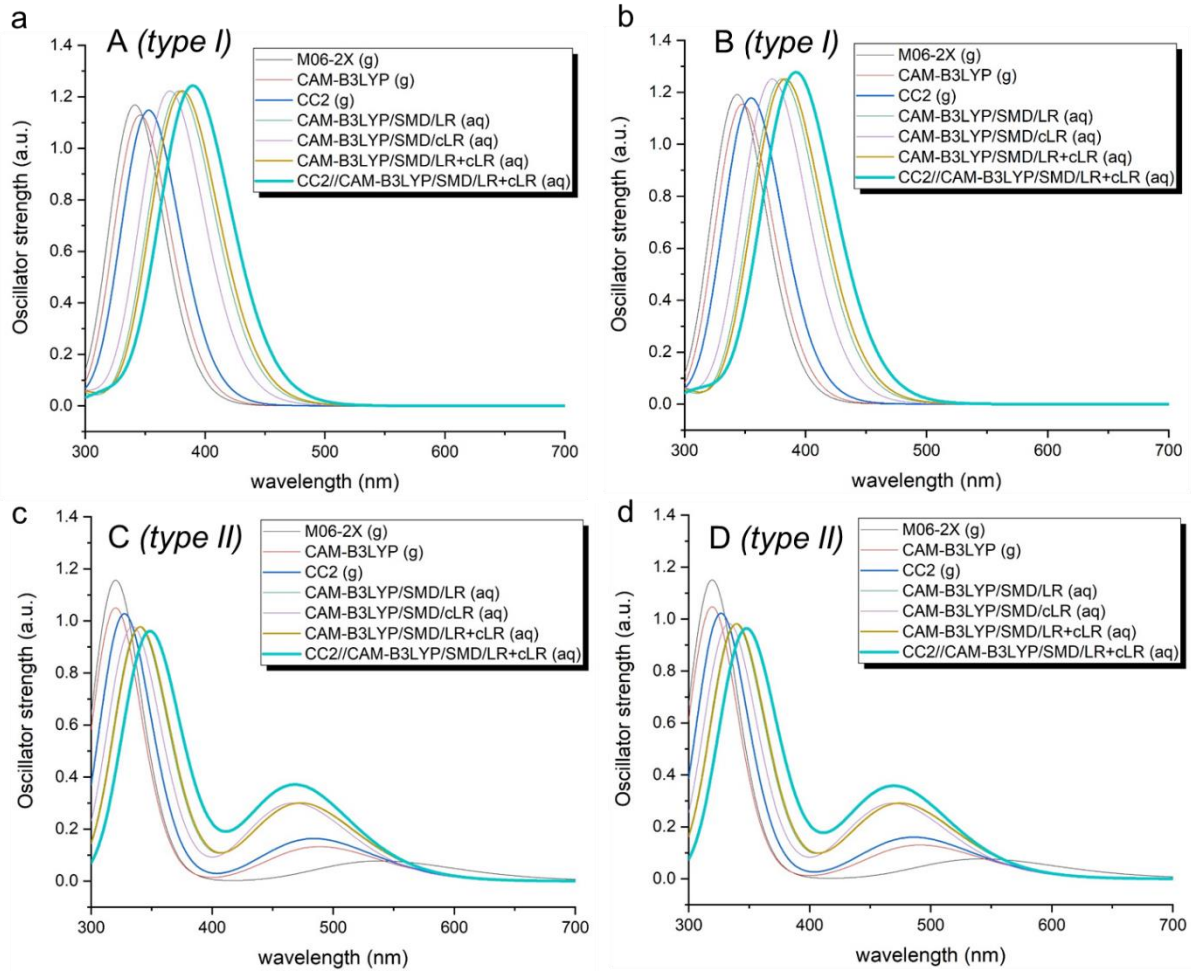

Figure S10.2. UV-Vis electronic absorption spectra of quasi-planar and distorted structures of ***E***

UV-Vis electronic absorption spectra of quasi-planar (type I, panels a,b) and distorted (type II, panels c,d) structures of the ***E*** form of compound **1** (structures are displayed in Figure S8.2) in the gas phase and aqueous environment. The simulated spectra (FWHM = 0.8 eV) were obtained by TD-DFT and CC2 methods using the 6-31++G(2df,2p) and def2-TZVPP basis sets, respectively, in the gas phase and by employing the LR, cLR and LR+cLR approaches combined with the SMD implicit solvation model at the CAM-B3LYP/6-31++G(2df,2p) level in the aqueous environment. The CC2//LR-cLR-CAM-B3LYP/SMD spectrum was obtained by shifting the LR-cLR-CAM-B3LYP spectrum (at the energy scale) by the difference between the gas phase CC2 and CAM-B3LYP spectra.

S10.a. Electronic transitions in the gas phase

In the gas phase, the M06-2X and CAM-B3LYP functionals were benchmarked against the CC2 method consistently using the def2-TZVPP basis set and the structures optimized at the M06-2X/6-31+G(d)/SMD (water) level (Figures S8.1 and S8.2).

Table S10.1. Gas phase VEEs for singlet ES of ***E***-H$^+$, ***Z***-H$^+$, ***Z***, and ***E***

The gas phase VEEs for the 3 lower singlet ES of ***E*-H$^+$**, ***Z*-H$^+$**, ***Z***, and ***E*** calculated at the *functional*/*basis set*//M06-2X/6-31+G(d) level of theory.

Species/ Functional/ Transition	MOs involved (unsigned relative weight)	Oscillator strength (*f*)	VEE (eV)	VEE (nm)
***E*-H$^+$**				
M06-2X/6-31++G(2df,2p)				
S0 -> S1	126 -> 127 (0.70)	1.42	2.74	453
S0 -> S2	125 -> 127 (0.69)	0.02	3.79	328
S0 -> S3	123 -> 127 (0.52) 121 -> 127 (0.38)	0.03	3.88	319
CAM-B3LYP/6-31++G(2df,2p)				
S0 -> S1	126 -> 127 (0.69)	1.37	2.73	454
S0 -> S2	125 -> 127 (0.69)	0.03	3.74	331
S0 -> S3	123 -> 127 (0.68)	0.04	3.83	323
CC2/def2-TZVPP				
S0 -> S1	126 -> 127 (0.97)	1.52	2.34	531
S0 -> S2	125 -> 127 (0.97)	0.02	3.36	370
S0 -> S3	123 -> 127 (0.70) 124 -> 127 (0.66)	0.08	3.54	350
***Z*-H$^+$**				
M06-2X/6-31++G(2df,2p)				
S0 -> S1	126 -> 127 (0.68)	0.61	2.77	448
S0 -> S2	125 -> 127 (0.49) 123 -> 127 (0.35) 121 -> 127 (0.25)	0.08	3.61	344
S0 -> S3	123 -> 127 (0.48) 124 -> 127 (0.31) 121 -> 127 (0.27)	0.00	3.78	328
CAM-B3LYP/6-31++G(2df,2p)				
S0 -> S1	126 -> 127 (0.68)	0.62	2.80	443
S0 -> S2	125 -> 127 (0.39) 123 -> 127 (0.49) 121 -> 127 (0.27)	0.06	3.61	344
S0 -> S3	123 -> 127 (0.43) 125 -> 127 (0.39) 121 -> 127 (0.27)	0.02	3.83	324

CC2/def2-TZVPP				
S0 -> S1	126 -> 127 (0.97)	0.68	2.40	518
S0 -> S2	125 -> 127 (0.81) 123 -> 127 (0.50)	0.06	3.30	376
S0 -> S3	123 -> 127 (0.80) 125 -> 127 (0.43) 124 -> 127 (0.31)	0.09	3.49	356
Z				
M06-2X/6-31++G(2df,2p)				
S0 -> S1	122 -> 127 (0.38) 126 -> 127 (0.50)	0.02	2.59	479
S0 -> S2	125 -> 127 (0.63)	0.06	4.08	304
S0 -> S3	120 -> 127 (0.22) 122 -> 127 (0.39) 126 -> 127 (0.47)	0.28	4.28	290
CAM-B3LYP/6-31++G(2df,2p)				
S0 -> S1	122 -> 127 (0.31) 126 -> 127 (0.53)	0.04	2.83	438
S0 -> S2	125 -> 127 (0.61)	0.06	4.09	303
S0 -> S3	120 -> 127 (0.22) 122 -> 127 (0.40) 126 -> 127 (0.38)	0.25	4.28	290
CC2/def2-TZVPP				
S0 -> S1	122 -> 127 (0.50) 126 -> 127 (0.66)	0.06	2.99	415
S0 -> S2	125 -> 127 (0.85)	0.08	3.30	313
S0 -> S3	124 -> 127 (0.31) 122 -> 127 (0.55) 126 -> 127 (0.56)	0.20	4.19	296
E (structure A)				
M06-2X/6-31++G(2df,2p)				
S0 -> S1	122 -> 127 (0.25) 125 -> 127 (0.56)	0.00	2.34	530
S0 -> S2	126 -> 127 (0.68)	1.17	3.63	341
S0 -> S3	123 -> 127 (0.24) 124 -> 127 (0.52)	0.03	4.56	272
CAM-B3LYP/6-31++G(2df,2p)				
S0 -> S1	122 -> 127 (0.22) 125 -> 127 (0.61)	0.00	2.62	475
S0 -> S2	126 -> 127 (0.68)	1.13	3.58	346
S0 -> S3	122 -> 127 (0.21) 123 -> 127 (0.21) 124 -> 127 (0.53)	0.03	4.50	276
CC2/def2-TZVPP				
S0 -> S1	122 -> 127 (0.76) 125 -> 127 (0.48)	0.00	2.62	473

S0 -> S2	126 -> 127 (0.95)	1.27	3.51	353
S0 -> S3	123 -> 127 (0.72) 125 -> 127 (0.34) 124 -> 127 (0.28)	0.03	4.20	295

S10.b. Electronic transitions in the aqueous environment.

Table S10.2. Basis set dependence of VEEs and oscillator strengths (*f*) for singlet ES of ***E*-H⁺**

Basis set dependence of VEEs and oscillator strengths (*f*) for the 3 lower singlet ES of ***E*-H⁺** calculated using the LR and cLR approaches at the TD-M06-2X/*basis set*/SMD (water)//M06-2X/6-31+G(d)/SMD (water) level of theory.

Basis set/ Transition	MOs involved in the transition (unsigned weight)	Oscillator strength (*f*)	VEE (eV)		VEE (nm)	
			LR	cLR	LR	cLR
6-31++G(2d,p)						
S0 -> S1		**1.60**	**2.64**	**2.74**	**470**	**452**
S0 -> S2		0.05	3.69	3.62	336	343
S0 -> S3		0.03	3.92	3.63	316	341
6-31++G(2df,2p)						
S0 -> S1	**126 -> 127 (0.70)**	**1.59**	**2.64**	**2.75**	**469**	**451**
S0 -> S2	123 -> 127 (0.69)	0.05	3.70	3.63	335	342
S0 -> S3	124 -> 127 (0.63) 125 -> 127 (0.27)	0.03	3.93	3.65	315	340
6-311++G(2df,2p)						
S0 -> S1		**1.60**	**2.64**	**2.74**	**470**	**452**
S0 -> S2		0.05	3.70	3.62	335	342
S0 -> S3		0.03	3.93	3.65	315	340

Table S10.3. VEEs and oscillator strengths (*f*) for singlet ES of ***E*-H⁺** in water

VEEs and oscillator strengths (*f*) for the 3 lower singlet ES of ***E*-H⁺** in water calculated at the TD-CAM-B3LYP/6-31++G(2df,2p)/SMD//M06-2X/6-31+G(d)/SMD level of theory. The CC2//LR-cLR-CAM-B3LYP/SMD values were obtained by shifting the LR-cLR-CAM-B3LYP data (at the energy scale) by the difference between the gas phase CC2 and CAM-B3LYP values.

Transition	LR-TD-DFT Oscillator strength (*f*)	VEE (eV)				VEE (nm)			
		TD-CAM-B3LYP			CC2// CAM-B3LYP	TD-CAM-B3LYP			CC2// CAM-B3LYP
		LR	cLR	LR+cLR	LR+cLR	LR	cLR	LR+cLR	LR+cLR
S0 -> S1	1.54	2.65	2.74	2.60	2.21	469	452	477	562
S0 -> S2	0.05	3.63	3.55	3.53	3.15	342	349	351	394
S0 -> S3	0.03	3.89	3.60	3.59	3.29	318	345	346	376

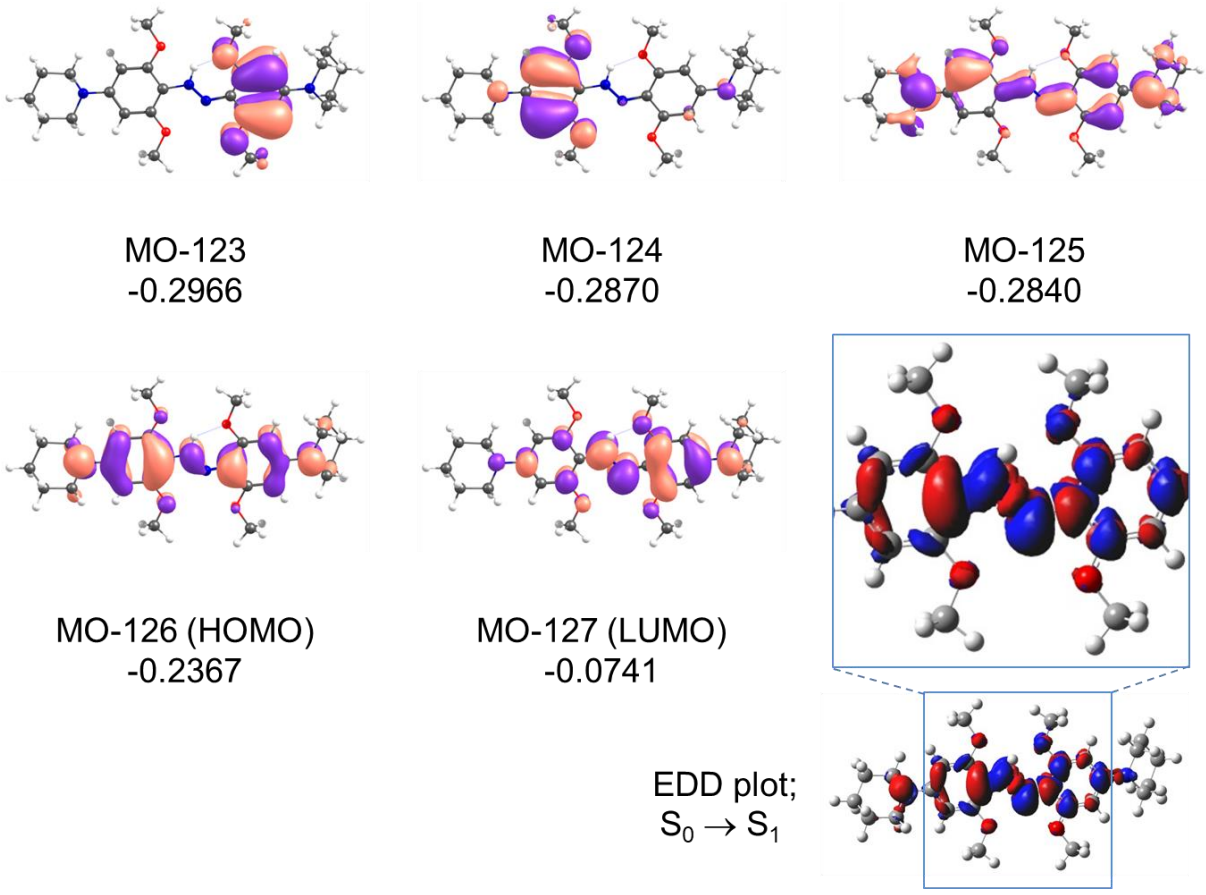

Figure S10.3. MOs involved in electronic transitions from GS to low-lying ES of ***E***-H^+

MOs involved in electronic transitions from GS to low-lying ES of ***E*-H$^+$** (orbital energies are given in a.u., contour value = 0.03) and the corresponding electron density difference plot (EDD, red = decrease, blue = increase, isovalue = 0.001 a.u.) for the transition to the bright state obtained at the (TD)-M06-2X/6-31++G(2df,2p)/SMD(water) level of theory.

Table S10.4. Basis set dependence of VEEs and oscillator strengths (*f*) for singlet ES of ***Z*-H⁺**

Basis set dependence of VEEs and oscillator strengths (*f*) for the 3 lower singlet ES of ***Z*-H⁺** calculated using the LR and cLR approaches at the TD-M06-2X/*basis set*/SMD (water)//M06-2X/6-31+G(d)/SMD (water) level of theory.

Basis set/ Transition	MOs involved in the transition (unsigned weight)	Oscillator strength (*f*)	VEE (eV)		VEE (nm)	
			LR	cLR	LR	cLR
6-31++G(2d,p)						
S0 -> S1		0.77	2.69	2.75	461.3	451.6
S0 -> S2		0.07	3.53	3.52	351.3	352.4
S0 -> S3		0.06	3.81	3.80	325.2	326.0
6-31++G(2df,2p)						
S0 -> S1	126 -> 127 (0.70)	0.77	2.69	2.75	460.6	451.0
S0 -> S2	123 -> 127 (0.53)	0.07	3.54	3.53	350.4	351.3
	124 -> 127 (0.26)					
	125 -> 127 (0.35)					
S0 -> S3	125 -> 127 (0.43)	0.05	3.81	3.80	325.9	326.4
	123 -> 127 (0.33)					
	121 -> 127 (0.31)					
6-311++G(2df,2p)						
S0 -> S1		0.77	2.69	2.74	461.6	452.0
S0 -> S2		0.07	3.54	3.53	350.5	351.6
S0 -> S3		0.06	3.81	3.80	325.8	326.4

Table S10.5. VEEs and oscillator strengths (*f*) for singlet ES of ***Z*-H⁺** in water

VEEs and oscillator strengths (*f*) for the 3 lower singlet ES of ***Z*-H⁺** in water calculated at the TD-CAM-B3LYP/6-31++G(2df,2p)/SMD//M06-2X/6-31+G(d)/SMD level of theory. The CC2//LR-cLR-CAM-B3LYP/SMD values were obtained by shifting the LR-cLR-CAM-B3LYP data (at the energy scale) by the difference between the gas phase CC2 and CAM-B3LYP values.

Transition	LR-TD-DFT Oscillator strength (*f*)	VEE (eV) TD-CAM-B3LYP			CC2// CAM-B3LYP	VEE (eV) TD-CAM-B3LYP			CC2// CAM-B3LYP
		LR	cLR	LR+cLR	LR+cLR	LR	cLR	LR+cLR	LR+cLR
S0 -> S1	0.77	2.71	2.76	2.67	2.27	458	449	465	547
S0 -> S2	0.06	3.48	3.46	3.44	3.13	357	359	361	396
S0 -> S3	0.06	3.83	3.76	3.74	3.40	324	330	332	365

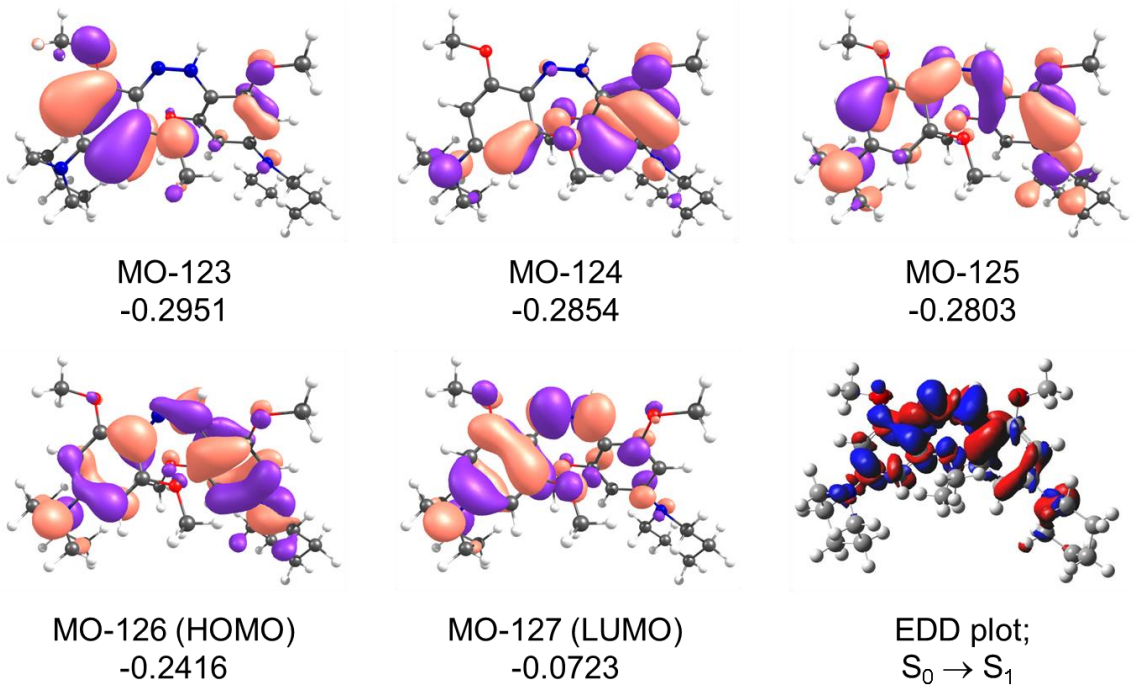

Figure S10.4. MOs involved in electronic transitions from GS to low-lying ES of ***Z*-H$^+$**

MOs involved in electronic transitions from GS to low-lying ESs of ***Z*-H$^+$** (orbital energies are given in a.u., contour value = 0.03) and the corresponding electron density difference plot (EDD, red = decrease, blue = increase, isovalue = 0.001 a.u.) for the transition to the bright state obtained at the (TD)-M06-2X/6-31++G(2df,2p)/SMD (water) level of theory.

Table S10.6. Basis set dependence of VEEs and oscillator strengths (*f*) for singlet ES of ***Z***

Basis set dependence of VEEs and oscillator strengths (*f*) for the 3 lower singlet ES of ***Z*** calculated using the LR and cLR approaches at the TD-M06-2X/*basis set*/SMD(water)//M06-2X/6-31+G(d)/SMD(water) level of theory.

Basis set/ Transition	MOs involved in the transition (unsigned weight)	Oscillator strength (*f*)	VEE (eV)		VEE (nm)	
			LR	cLR	LR	cLR
6-31++G(2d,p)						
S0 -> S1		0.05	2.60	2.61	476.7	475.3
S0 -> S2		0.09	3.74	3.72	331.2	333.0
S0 -> S3		0.27	3.92	3.91	316.0	316.7
6-31++G(2df,2p)						
S0 -> S1	122 -> 127 (0.40) 126 -> 127 (0.50)	0.04	2.59	2.60	478.7	477.3
S0 -> S2	125 -> 127 (0.63)	0.09	3.76	3.74	329.9	331.7
S0 -> S3	120 -> 127 (0.37) 122 -> 127 (0.30) 126 -> 127 (0.47)	0.27	3.94	3.93	315.0	315.8
6-311++G(2df,2p)						
S0 -> S1		0.04	2.59	2.60	478.3	476.8
S0 -> S2		0.09	3.76	3.74	329.9	331.7
S0 -> S3		0.27	3.93	3.92	315.3	316.0

Table S10.7. VEEs and oscillator strengths (*f*) for singlet ES of ***Z*** in water.

VEEs and oscillator strengths (*f*) for the 3 lower singlet ES of ***Z*** in water calculated at the TD-CAM-B3LYP/6-31++G(2df,2p)/SMD//M06-2X/6-31+G(d)/SMD level of theory. The CC2//LR-cLR-CAM-B3LYP/SMD values were obtained by shifting the LR-cLR-CAM-B3LYP data (at the energy scale) by the difference between the gas phase CC2 and CAM-B3LYP values.

Transition	LR-TD-DFT Oscillator strength (*f*)	VEE (eV) TD-CAM-B3LYP			CC2// CAM-B3LYP	VEE (eV) TD-CAM-B3LYP			CC2// CAM-B3LYP
		LR	cLR	LR+cLR	LR+cLR	LR	cLR	LR+cLR	LR+cLR
S0 -> S1	0.08	2.78	2.79	2.77	2.94	446	444	447	422
S0 -> S2	0.09	3.73	3.71	3.69	3.56	332	334	336	348
S0 -> S3	0.22	3.97	3.97	3.94	3.86	312	312	314	321

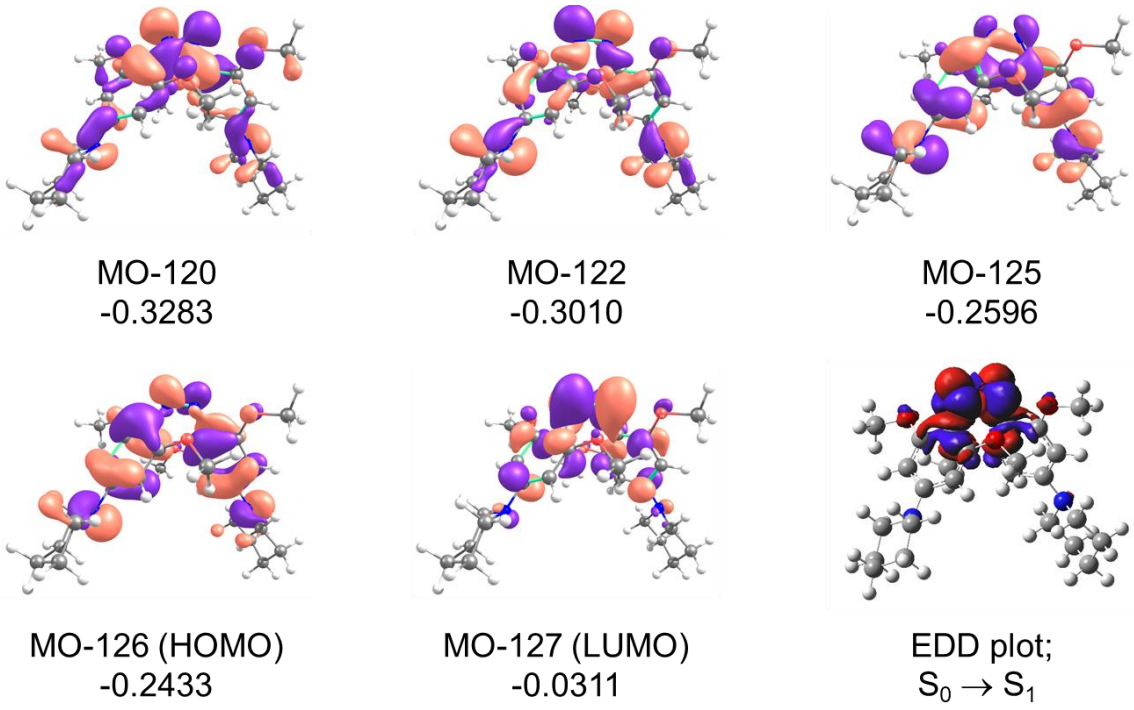

Figure S10.5. MOs involved in electronic transitions from GS to low-lying ES of ***Z***

MOs involved in electronic transitions from GS to low-lying ES of ***Z*** (orbital energies are given in a.u., contour value = 0.03) and the corresponding electron density difference plot (EDD, red = decrease, blue = increase, isovalue = 0.001 a.u.) for the transition to the bright state obtained at the (TD)-M06-2X/6-31++G(2df,2p)/SMD (water) level of theory.

Table S10.8. Basis set dependence of VEEs and oscillator strengths (*f*) for singlet ES of ***E***

Basis set dependence of VEEs and oscillator strengths (*f*) for the 3 lower singlet ES of ***E*** (structure A, see Figure SX.2) calculated using the LR and cLR approaches at the TD-M06-2X/*basis set*/SMD (water)//M06-2X/6-31+G(d)/SMD (water) level of theory.

Basis set/ Transition	MOs involved in the transition (unsigned weight)	Oscillator strength (*f*)	VEE (eV)		VEE (nm)	
			LR	cLR	LR	cLR
6-31++G(2d,p)						
S0 -> S1		0.00	2.57	2.56	483.1	484.4
S0 -> S2		**1.27**	**3.32**	**3.39**	**373.6**	**366.2**
S0 -> S3		0.06	4.33	4.27	286.5	290.3
6-31++G(2df,2p)						
S0 -> S1	122 -> 127 (0.48) 125 -> 127 (0.41)	0.00	2.53	2.52	489.9	491.3
S0 -> S2	**126 -> 127 (0.69)**	**1.27**	**3.33**	**3.40**	**372.6**	**365.2**
S0 -> S3	123 -> 127 (0.34) 124 -> 127 (0.51) 125 -> 127 (0.24)	0.06	4.34	4.29	285.4	289.2
6-311++G(2df,2p)						
S0 -> S1		0.00	2.54	2.53	488.1	489.4
S0 -> S2		**1.27**	**3.32**	**3.39**	**373.5**	**366.0**
S0 -> S3		0.06	4.34	4.28	285.8	289.5

Table S10.9. VEEs and oscillator strengths (*f*) for singlet ES of ***E***

VEEs and oscillator strengths (*f*) for the 3 lower singlet ES of quasi-planar (A,D) and distorted (B,C) structures of ***E*** in water calculated at the TD-CAM-B3LYP/6-31++G(2df,2p)/SMD//M06-2X/6-31+G(d)/SMD level of theory. The CC2//LR-cLR-CAM-B3LYP/SMD values were obtained by shifting the LR-cLR-CAM-B3LYP data (at the energy scale) by the difference between the gas phase CC2 and CAM-B3LYP values.

Transition	LR-TD-DFT Oscillator strength (*f*)	VEE (eV) TD-CAM-B3LYP			CC2// CAM-B3LYP	VEE (eV) TD-CAM-B3LYP			CC2// CAM-B3LYP
		LR	cLR	LR+cLR	LR+cLR	LR	cLR	LR+cLR	LR+cLR
Structure A									
S0 -> S1	0.00	2.80	2.79	2.79	2.80	443	444	445	443
S0 -> S2	1.22	3.28	3.34	3.25	3.18	378	371	381	390
S0 -> S3	0.06	4.27	4.20	4.19	3.89	290	295	296	319
Structure B									
S0 -> S1	0.29	2.62	2.64	2.61	2.64	474	469	475	470
S0 -> S2	0.98	3.66	3.72	3.65	3.56	339	333	340	348
S0 -> S3	0.04	4.26	4.23	4.21	3.91	291	293	294	317
Structure C									
S0 -> S1	0.30	2.62	2.65	2.62	2.65	472	468	473	469
S0 -> S2	0.98	3.65	3.71	3.64	3.55	340	334	341	349
S0 -> S3	0.03	4.27	4.25	4.23	3.93	290	292	293	316
Structure D									
S0 -> S1	0.00	2.79	2.79	2.78	2.78	444	445	446	445
S0 -> S2	1.25	3.26	3.33	3.24	3.16	381	373	383	392
S0 -> S3	0.06	4.29	4.25	4.23	3.94	289	292	293	315

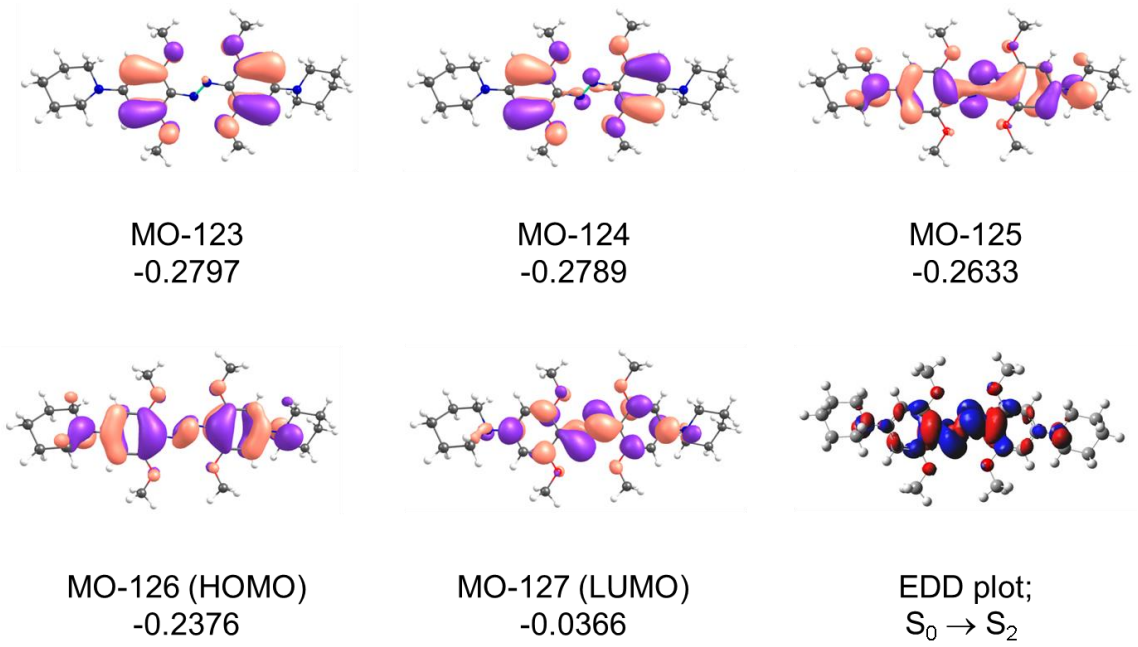

Figure S10.6. MOs involved in electronic transitions from GS to low-lying ES of ***E***

MOs involved in electronic transitions from GS to low-lying ES of ***E*** (structure A in Figure S8.2; orbital energies are given in a.u.) and the corresponding electron density difference plot (EDD, red = decrease, blue = increase, isovalue = 0.001 a.u.) for the transition to the bright state (S_2) obtained at the (TD)-M06-2X/6-31++G(2df,2p)/SMD(water) level of theory.

S10.c. The doubly protonated E-form (E-2H^{2+}) and its electronic transitions

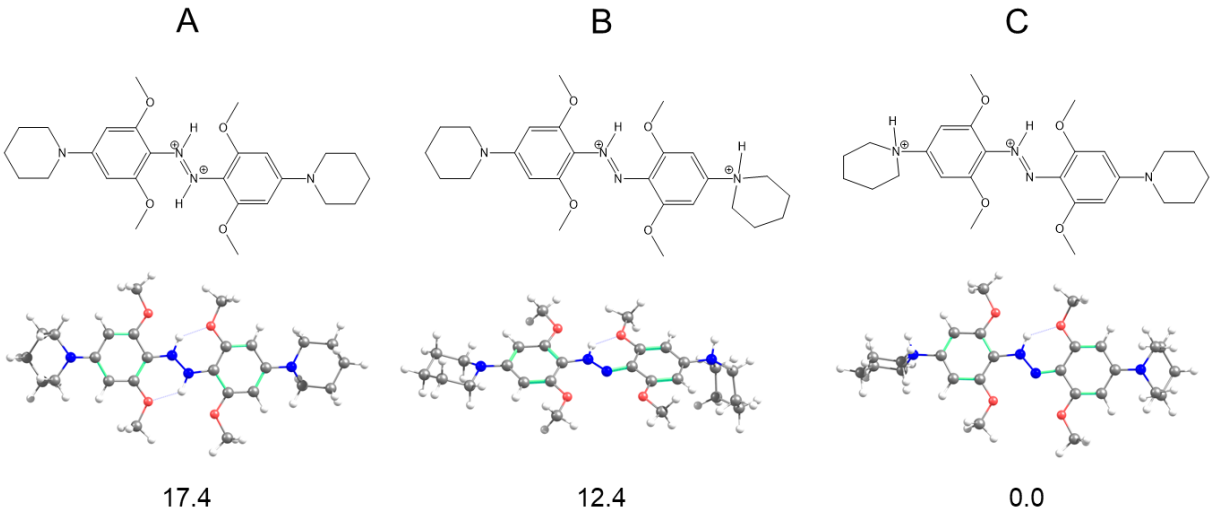

Figure S10.7. Structures of the doubly protonated *E*-form (*E*-2H^{2+}).

Structures of the doubly protonated ***E*-form (*E*-2H^{2+})** optimized at the M06-2X/6-31+G(d)/SMD (water) level of theory. Relative energies with respect to the most stable isomer are given in kcal/mol.

Table S10.10. Basis set dependence of VEEs and oscillator strengths (*f*) for singlet ES of *E*-2H^{2+}

Basis set dependence of VEEs and oscillator strengths (*f*) for the 3 lower singlet ES of ***E*-2H^{2+}** (structure C in Figure S10.7) calculated using the LR and cLR approaches at the TD-M06-2X/*basis set*/SMD (water)//M06-2X/6-31+G(d)/SMD (water) level of theory.

Basis set/ Transition	MOs involved in the transition (unsigned weight)	Oscillator strength (*f*)	VEE (eV)		VEE (nm)	
			LR	cLR	LR	cLR
6-31++G(2d,p)						
S0 -> S1		**1.56**	**2.93**	**3.06**	**424**	**406**
S0 -> S2		0.06	3.60	3.54	345	350
S0 -> S3		0.00	4.09	4.06	316	319
6-31++G(2df,2p)						
S0 -> S1	**126 -> 127 (0.70)**	**1.56**	**2.93**	**3.06**	**423**	**405**
S0 -> S2	124 -> 127 (0.68)	0.06	3.61	3.55	344	349
S0 -> S3	121 -> 127 (0.63)					309
	122 -> 127 (0.15)	0.00	4.04	4.01	307	
6-311++G(2df,2p)						
S0 -> S1		**1.56**	**2.93**	**3.06**	**423**	**406**
S0 -> S2		0.05	3.60	3.55	344	350
S0 -> S3		0.00	4.05	4.02	306	308

Table S10.11. VEEs and oscillator strengths (*f*) for singlet ES of ***E*-2H^{2+}** in water.

VEEs and oscillator strengths (*f*) for the 3 lower singlet ES of ***E*-2H^{2+}** in water calculated at the TD-CAM-B3LYP/6-31++G(2df,2p)/SMD//M06-2X/6-31+G(d)/SMD level of theory. The CC2//LR-cLR-CAM-B3LYP/SMD values were obtained by shifting the LR-cLR-CAM-B3LYP data (at the energy scale) by the difference between the gas phase CC2 and CAM-B3LYP values.

Transition	LR-TD-DFT Oscillator strength (*f*)	VEE (eV) TD-CAM-B3LYP			CC2// CAM-B3LYP	VEE (eV) TD-CAM-B3LYP			CC2// CAM-B3LYP
		LR	cLR	LR+cLR	LR+cLR	LR	cLR	LR+cLR	LR+cLR
S0 -> S1	1.51	2.94	3.06	2.92	2.67	421	405	424	465
S0 -> S2	0.06	3.54	3.48	3.46	3.24	351	356	359	383
S0 -> S3	0.04	4.10	3.83	3.82	3.74	302	324	325	332

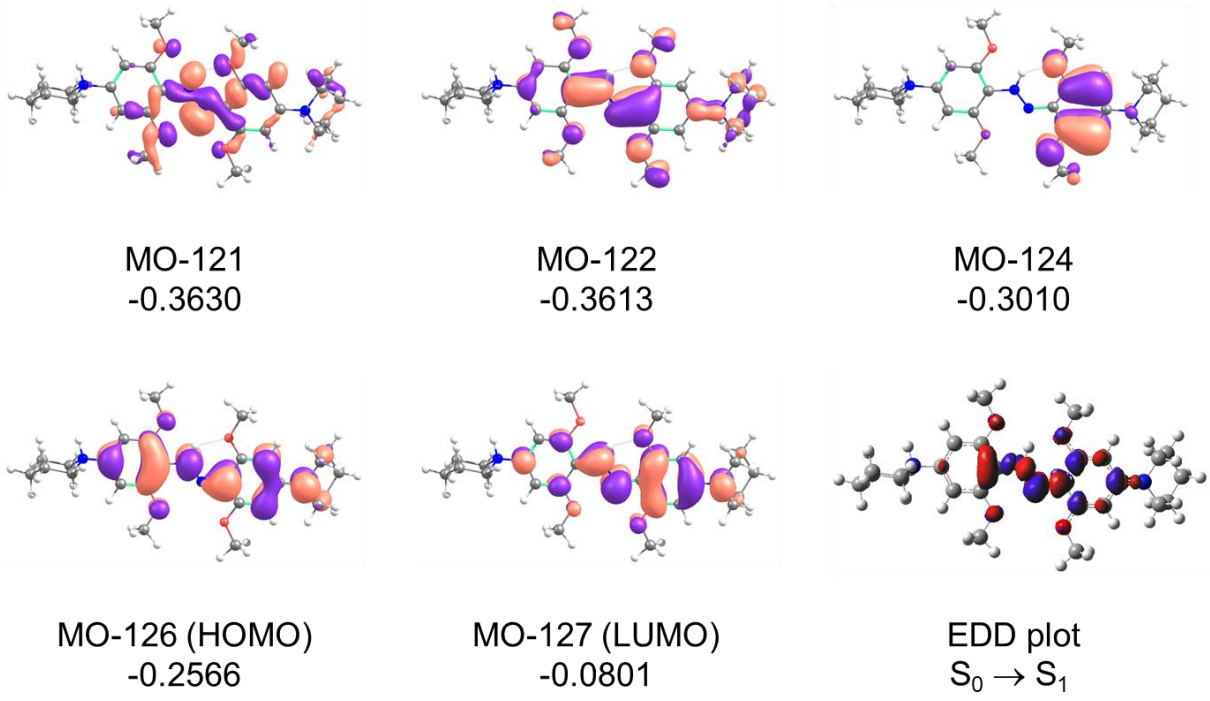

Figure S10.8. MOs involved in electronic transitions from GS to low-lying ES of ***E*-2H^{2+}**

MOs involved in electronic transitions from GS to low-lying ESs of ***E*-2H^{2+}** (orbital energies are given in a.u., contour value = 0.03) and the corresponding electron density difference plot (EDD, red = decrease, blue = increase, isovalue = 0.001 a.u.) for the transition to the bright state obtained at the (TD)-M06-2X/6-31++G(2df,2p)/SMD (water) level of theory.

*S10.d Charge transfer character of electronic transitions in **E**, **E**-H$^+$, and **E**-2H^{2+}.*

The strong CT character of the $S_0 \rightarrow S_1$ transition in ***E*-H$^+$** was deduced from the electron density difference (EDD) plots indicating significantly larger charge redistribution in the case of ***E*-H$^+$** compared to ***E*** and ***E*-2H^{2+}**. The spatial extent associated with a CT electronic transition can be described by the D_{CT} index proposed by Ciofini and colleagues,[45] defined as the distance between the barycenters of the density depletion and the density increment zones evaluated from the electron densities for the GS and the ES of interest. The associated fraction of charge transferred (q_{CT}) can also be determined. Although the transferred charge appears to be similar for all forms, the distance of the CT between the barycenters (D_{CT}) index confirms the transition in ***E*-H$^+$** has the strongest CT character (Table S10.12).

Table S10.12. Electron density difference (EDD) plots, DCT and q_{CT} indices of relevant electronic transitions in for ***E***, ***E*-H$^+$**, and ***E*-2H^{2+}**.

System/transition	EDD plot	D_{CT} (Å)	q_{CT} (a.u.)
E $S_0 \rightarrow S_2$	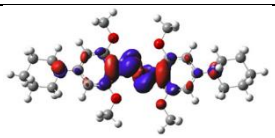	0.05	0.59
E-H$^+$ $S_0 \rightarrow S_1$	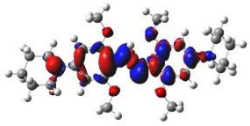	2.41	0.56
E-2H^{2+} $S_0 \rightarrow S_1$	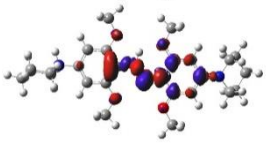	1.24	0.53

Systems were evaluated at the CAM-B3LYP/6-31++G(2df,2p)/SMD(LR, solvent=water) level of theory.

S11. Consideration of explicit water molecules and dynamics.

S11.1. Static model

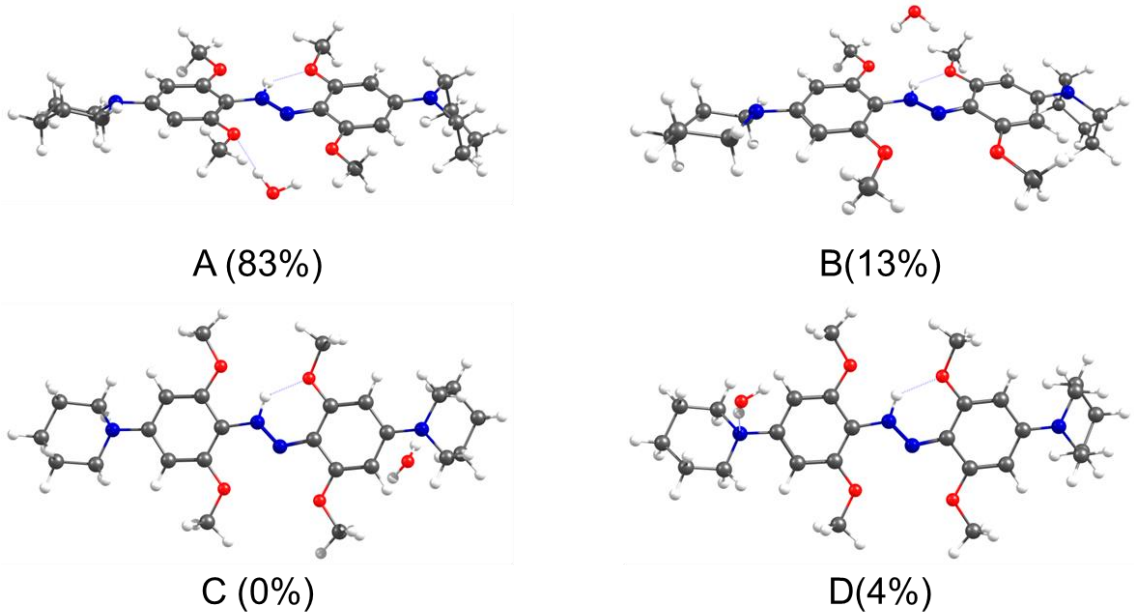

Figure S11.1. Structures and Boltzmann distribution probabilities of *E*-H^+...H_2O systems.

Structures and Boltzmann distribution probabilities (T = 298 K) of ***E*-H^+…H_2O** systems obtained at the M06-2X/6-31+G(d)/SMD (water) level of theory. The explicit water molecules prefer to form hydrogen bonds with oxygen atoms of the methoxy groups not involved in the intramolecular hydrogen bond (structure A).

S11.2 Dynamic model

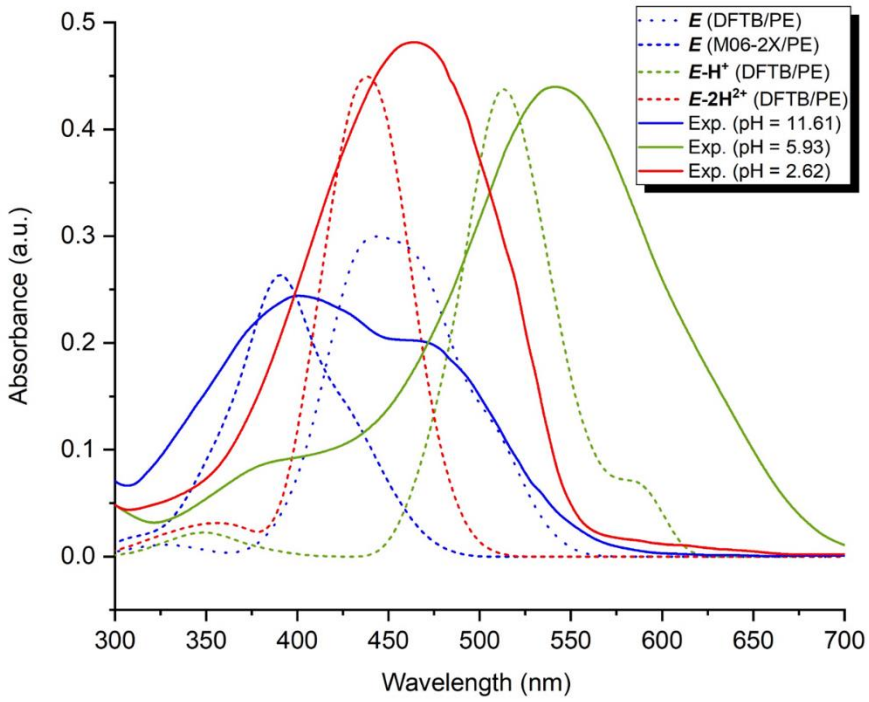

Figure S11.2. Comparison of experimental and simulated UV-Vis spectra of ***E***, ***E***-H^+ and ***E***-$2H^{2+}$

Comparison of experimental and simulated UV-Vis spectra of ***E***, ***E***-$\mathbf{H}^+$ and ***E***-$\mathbf{2H}^{2+}$ forms in water obtained from polarizable embedding (PE) calculations performed at the CAM-B3LYP/6-311+G(d) level using 50 snapshots from 1 ns QM/MM/EE trajectories using DFTB and M06-2X/6-31+G(d) methods to describe the solute molecule respectively, and the SPC-Fw force-field for the water solvent. All experimental absorption intensities were scaled by a factor of 0.7 to match the experimental and theoretical maxima for the ***E***-$\mathbf{H}^+$ form. The theoretical spectra represent the histogram curve of average oscillator strengths using bin-width of 20 nm.

Comment: Whereas the DFTB/PE approach reasonably reproduces the experimental spectra of ***E***-$\mathbf{H}^+$ and ***E***-$\mathbf{2H}^+$ forms, in the case of the ***E*** form it only captures the long wavelength band (450-500 nm) observed in experiment. On the other hand, the M06-2X/PE approach correctly predicts the higher intensity of a short wavelength band with the maximum at about 400 nm, and the spectrum exhibits a long wavelength tail (in agreement with the spectra predicted by using implicit solvation model, see Figure 1a), although the separation of the two bands is much less pronounced compared to experiment. The differences between the DFTB/PE and M06-2X/PE approaches are apparently related to different preferences for quasi-planar and distorted structures in the sampling during the MD simulations (see Figures S11.3 and S11.4).

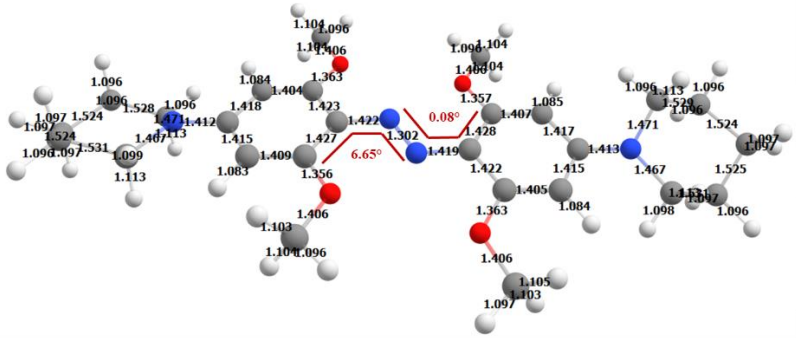

SMD excitation energies (CAM-B3LYP/6-311+G(d)) for E-from at DFTB gas phase minimized geometry

	Excitation energy	Oscillator strength
S0→S1	469.71 nm (2.640 eV)	0.0271
S0→S2	412.88 nm (3.003 eV)	1.4429
S0→S3	301.06 nm (4.118 eV)	0.0576

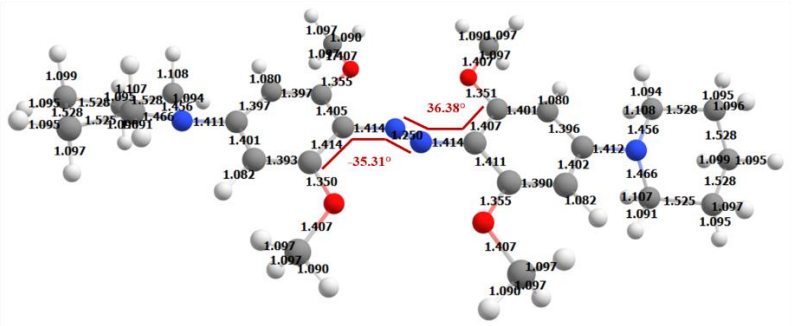

SMD excitation energies (CAM-B3LYP/6-311+G(d)) for E-from at gas phase M06-2X/6-31G(d) optimized geometry

	Excitation energy	Oscillator strength
S0→S1	431.18 nm (2.875 eV)	0.0002
S0→S2	372.07 nm (3.332 eV)	1.1192
S0→S3	289.78 nm (4.279 eV)	0.0619

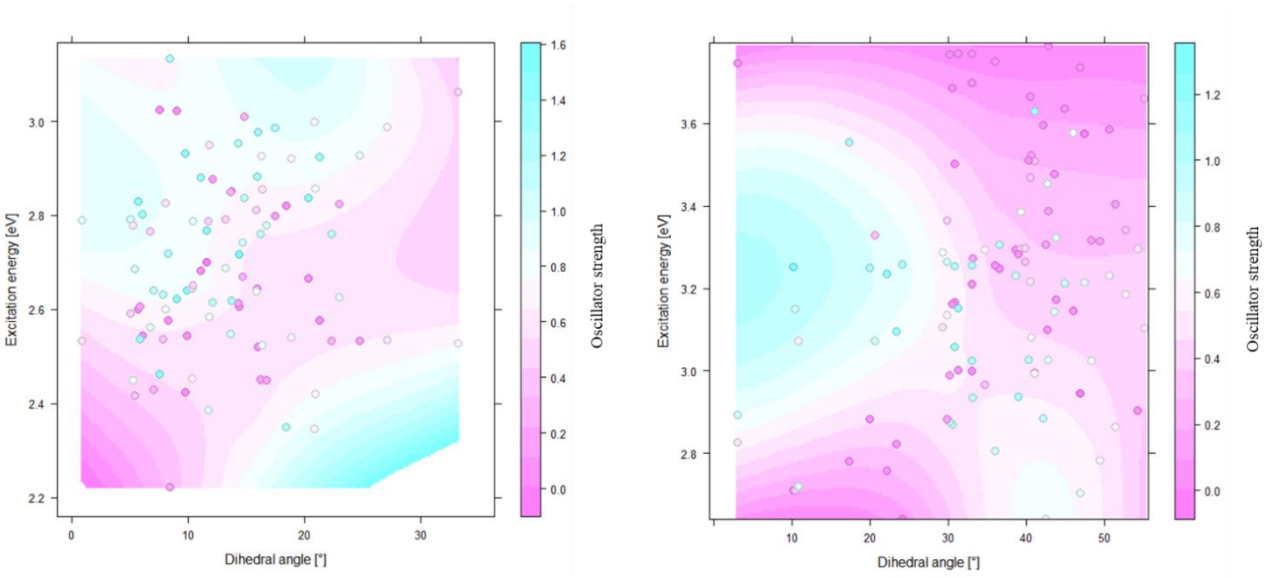

Figure S11.3. DFTB and M06-2X gas phase structures of ***E*** and corresponding VEEs for solvated systems.

Comparison of the DFTB and M06-2X gas phase structures of ***E*** and corresponding VEEs for solvated systems (SMD model, top panels). Sampling of the average of the absolute dihedral angles in the DFTB/SPC-Fw (bottom left) and M06-2X/6-31G(d)/SPC-Fw (bottom right) MD simulations.

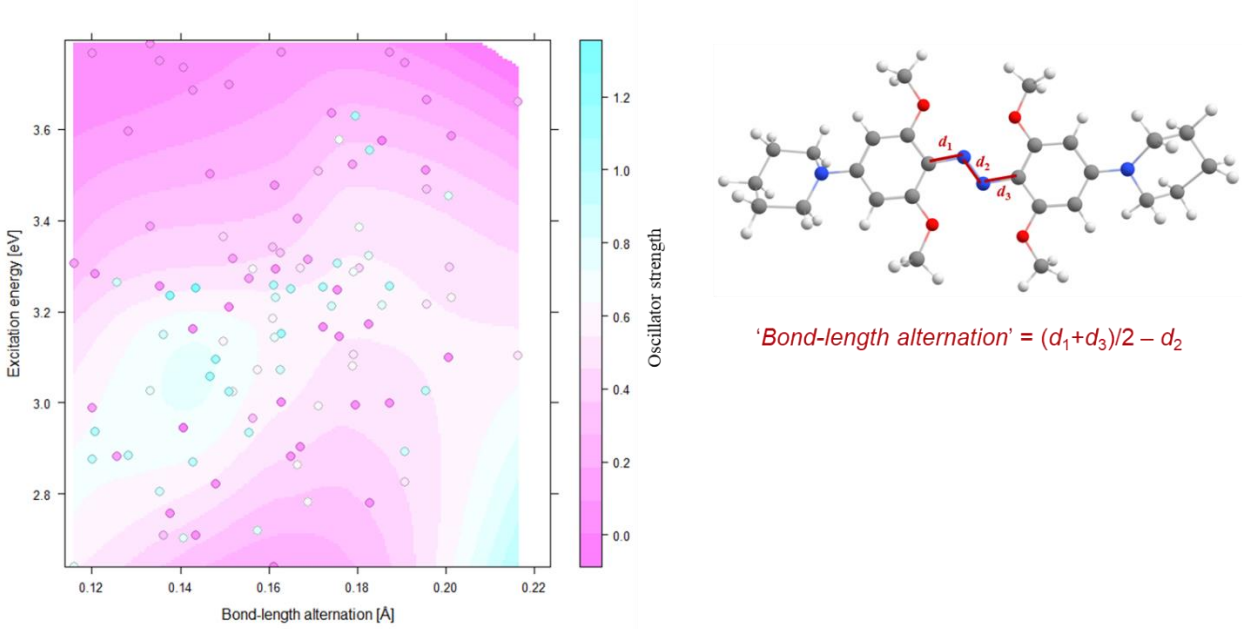

Figure S11.4. Sampling of the bond-length alternation (BLA) parameter.

Sampling of the bond-length alternation (BLA) parameter in the M06-2X/6-31G(d)/SPC-Fw MD simulations. The MD average is 0.163 ± 0.003 Å which is close to the SMD/M06-2X/6-31G(d) value of 0.151 Å, unlike the much smaller DFTB/SPC-Fw value (0.118 Å ± 0.004 Å) indicative for more efficient π-conjugation in quasi-planar structures.

Table S11.1. Parameters used for polarizable embedding calculations.

Atom coordinates (n) and distributed atom site-localized charges (q), dipole moments (μ), quadrupole moments (Q) and dipole-dipole polarizabilities (α) of water molecule and Cl^- counterion, used for polarizable embedding calculations. Properties were calculated at the B3LYP/aug-cc-pVTZ level and all values are listed in a.u.

	O	H1	H2	Cl^-
n_i [a]	0.0000, 0.0000, -0.1183	-1.3951, 0.4570, 0.9385	1.3951, -0.4570, 0.9385	0.0000, 0.0000, 0.0000
q	-0.7018	0.3509	0.3509	-1.000
μ_i [a]	0.0000, 0.0000, 0.2397	0.1448, -0.0474, -0.1381	-0.1448, 0.0474, -0.1381	0.0000, 0.0000, 0.0000
Q_{ii} [b]	-3.5621, -4.6247, -4.1353	-0.2348, -0.4919, -0.3385	-0.2348, -0.4919, -0.3385	-13.207, -13.207, -13.207
Q_{ij} [c]	-0.3899, 0.0000, 0.0000	-0.0944, -0.2348, 0.0769	-0.0944, 0.2348, -0.0769	0.000, 0.000, 0.000
α_{ii} [b]	5.3029, 5.6313, 5.4815	2.4424, 1.9294, 2.0835	2.4424, 1.9294, 2.0835	28.780, 28.780, 28.780
α_{ij} [c]	0.1203, -0.0008, 0.0024	-0.1889, -1.1170, 0.3675	-0.1889, 1.1170, -0.3675	0.000, 0.000, 0.000

[a] The index *i* runs over *x*, *y*, and *z*; [b] The double index *ii* runs over *xx*, *yy*, and zz; [c] The double index *ij* runs over *xy*, *xz*, and *yz*.

S12. Excited state structure of ***E*-H⁺** and ESIPT

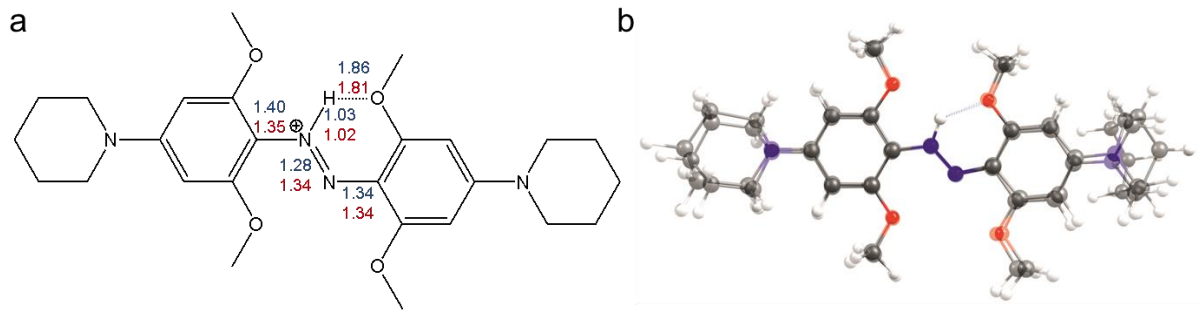

Figure S12.1. GS and ES (S1) structures of ***E*-H⁺**

(a) Comparison of GS and ES (S1) structures of ***E*-H⁺** (bond lengths are in Å, GS – blue, ES – red) and (b) superimposed GS and ES structures optimized at the (TD)-M06-2X/6-31+G(d)/SMD (water) level.

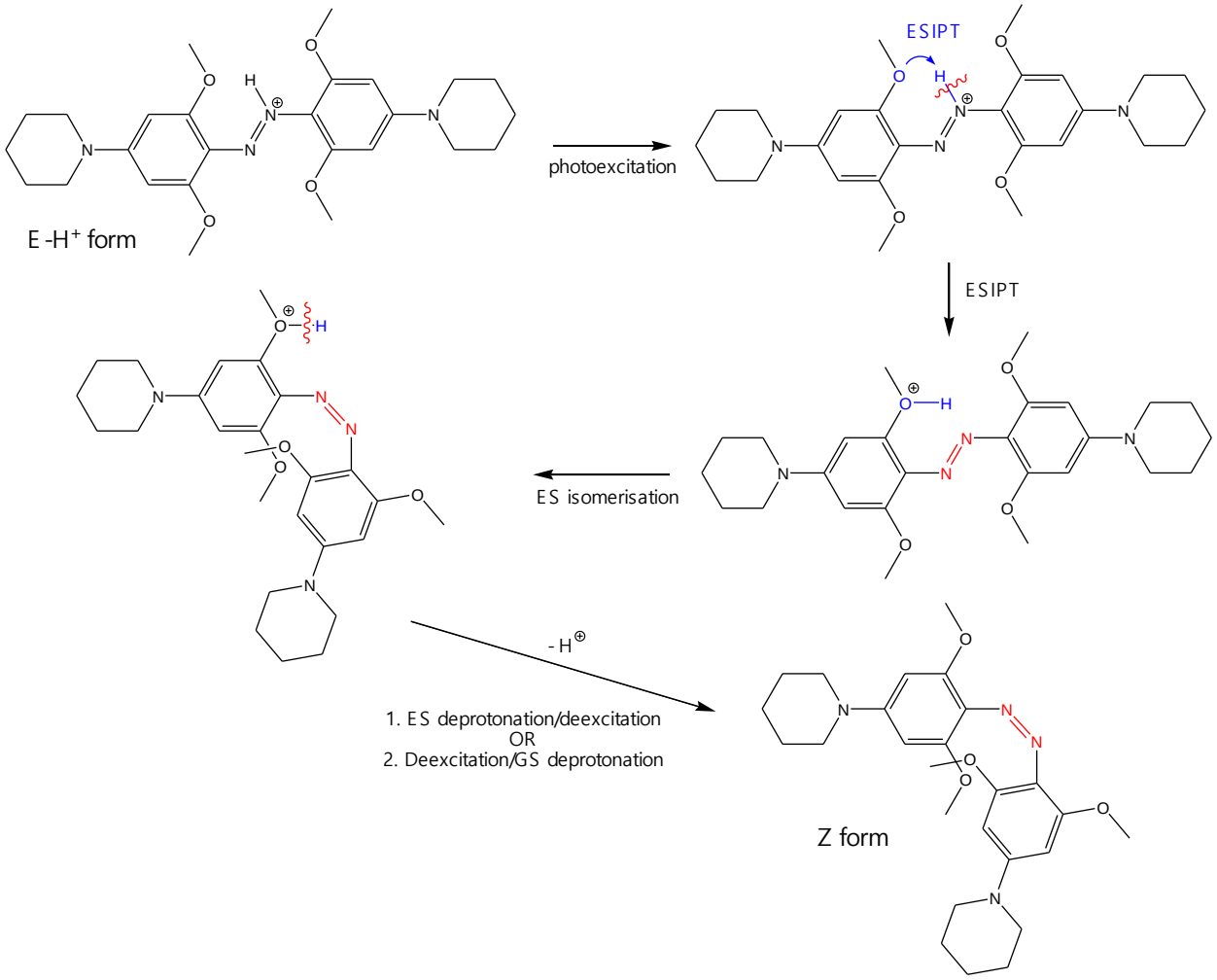

Scheme S12.1. Possible ESIPT pathways.

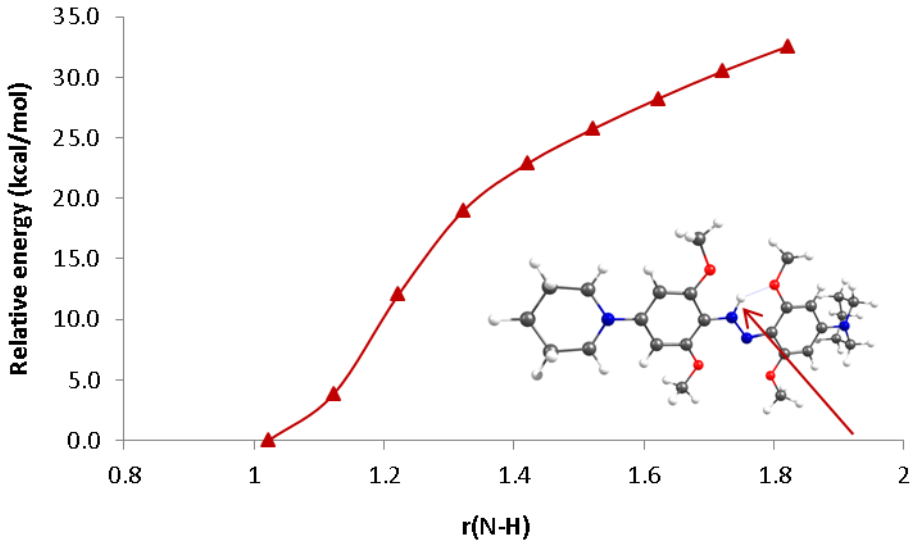

Figure S12.2. Energetics of the ESIPT process

Dependence of the relative energy of the ES (S_1) structures of ***E*-H**$^+$ on the N–H bond distance (in Å) for the ESIPT process obtained by a relaxed scan at the TD-M06-2X/6-31+G(d)/SMD level of theory.

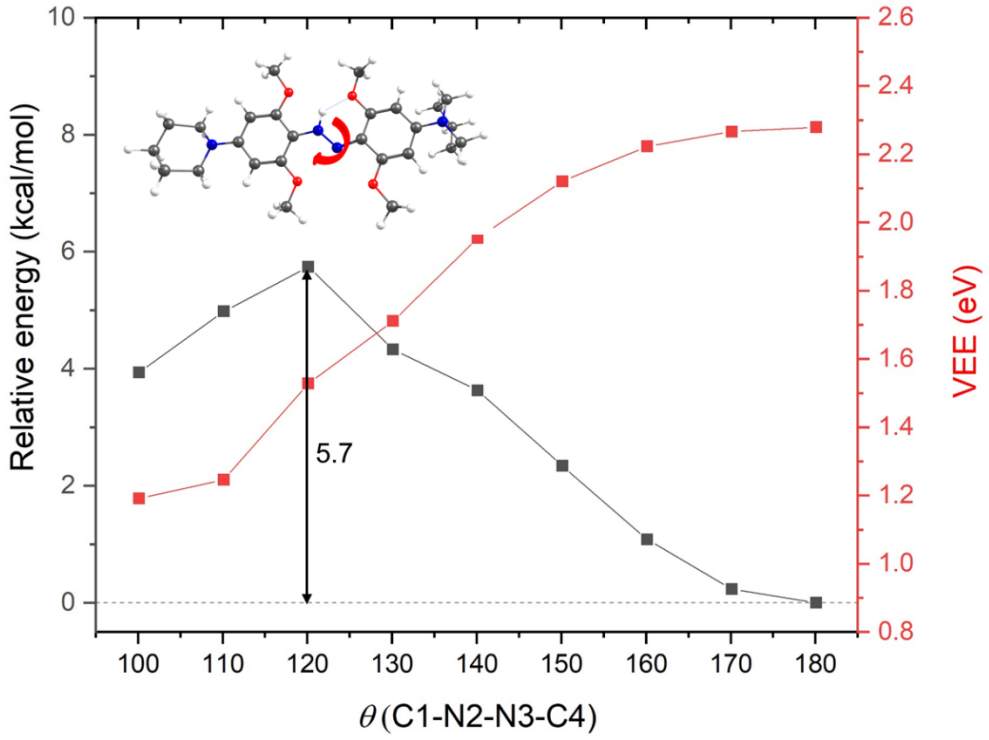

Figure S12.3. Energetics of N=N rotation in S_1.

Dependence of the relative energy (in kcal/mol, black points) of the S_1 structures of ***E*-H**$^+$ (w.r.t. to the S_1 structure optimized by TD-M06-2X) on the torsion angle θ(C1-N2-N3-C4) obtained at the SF-TD-BHHLYP/6-31++G(d,p)/SMD level of theory. For angles ranging from 180 to 130°, the structures were obtained by a relaxed scan employing TD-M06-2X. Structures with θ = 100-120° were obtained by twisting the 130° structure while keeping the remaining internal coordinates frozen. The red points show SF-TD-DFT VEEs (in eV) for the $S_0 \rightarrow S_1$ transition.

Comments:

1. Upon excitation, ***E*-H$^+$** retains the planarity of the central part of a molecule (Figure S12.1). The N=N bond length notably increases as a result of the HOMO-LUMO ($\pi\pi^*$) transition (see Figure SX.6) "preparing" the system for the isomerization, although the hydrogen bond still stabilizes the structure.
2. The activation energy for the proton transfer in the S_1 state of ***E*-H$^+$** is high (Figure S12.2), so the ESIPT process is improbable.
3. The isomerization in the S_1 state of ***E*-H$^+$** leading to the CI region appears to have a small barrier (ca. 6 kcal/mol) related to the breaking of the H-bond (Figure S12.3), which lowers the QY of photoisomerization compared to the ***E*** form.

S13. Thermal isomerization of protonated forms (*Z*-H$^+$ ↔ *E*-H$^+$)

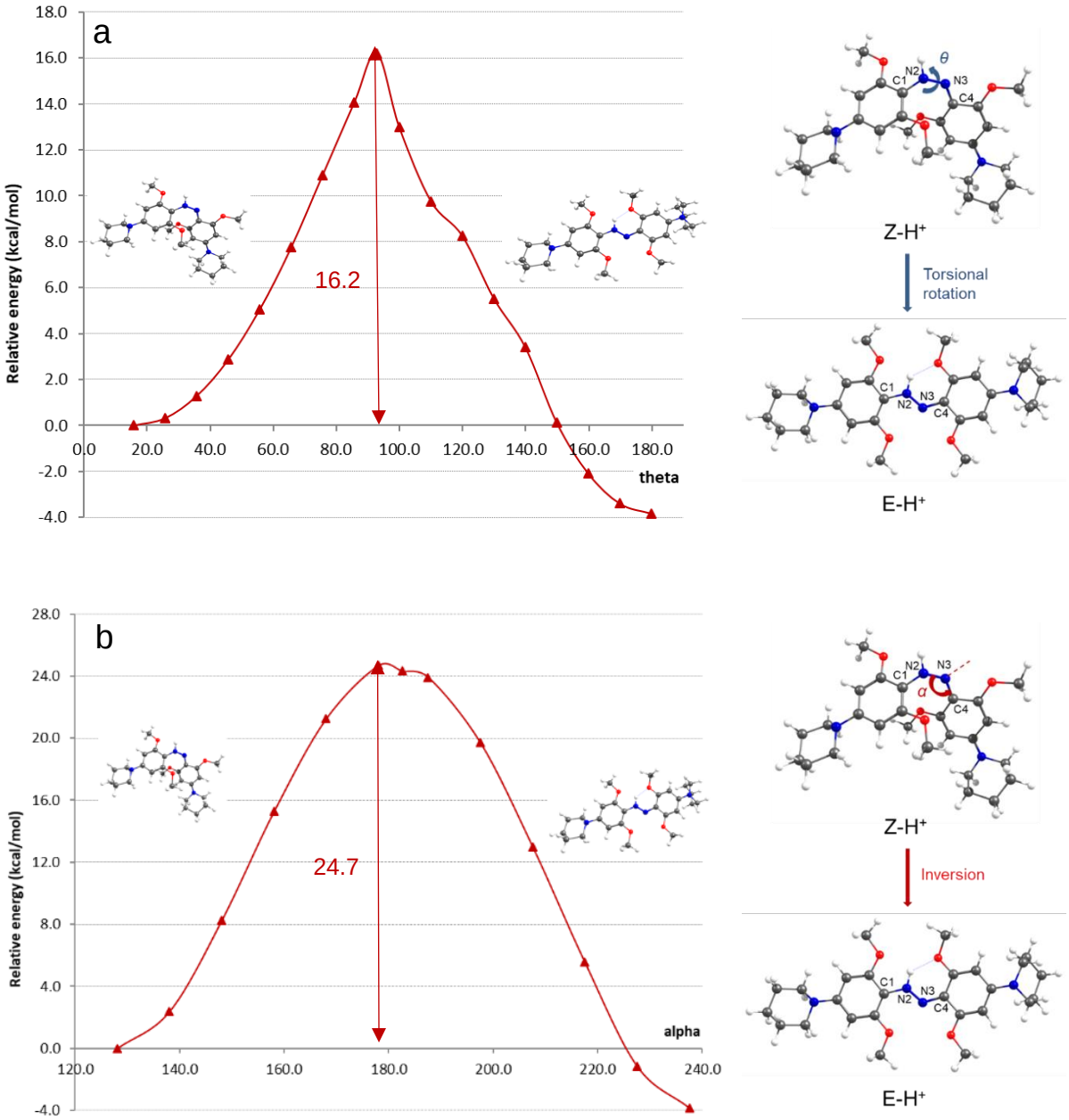

Figure S13.1. Energetics of thermal isomerization (*Z*-H$^+$ ↔ *E*-H$^+$).

Relaxed scans for isomerization of ***E*-H$^+$** to ***Z*-H$^+$** obtained at the M06-2X/ 6-31+G(d)/SMD (water) level of theory. (a) Torsional rotation (dihedral angle θ(C1-N2-N3-C4)), (b) inversion (bond angle α(N2-N3-C4)).

S14. Thermal isomerization of neutral forms (*Z* ↔ *E*)

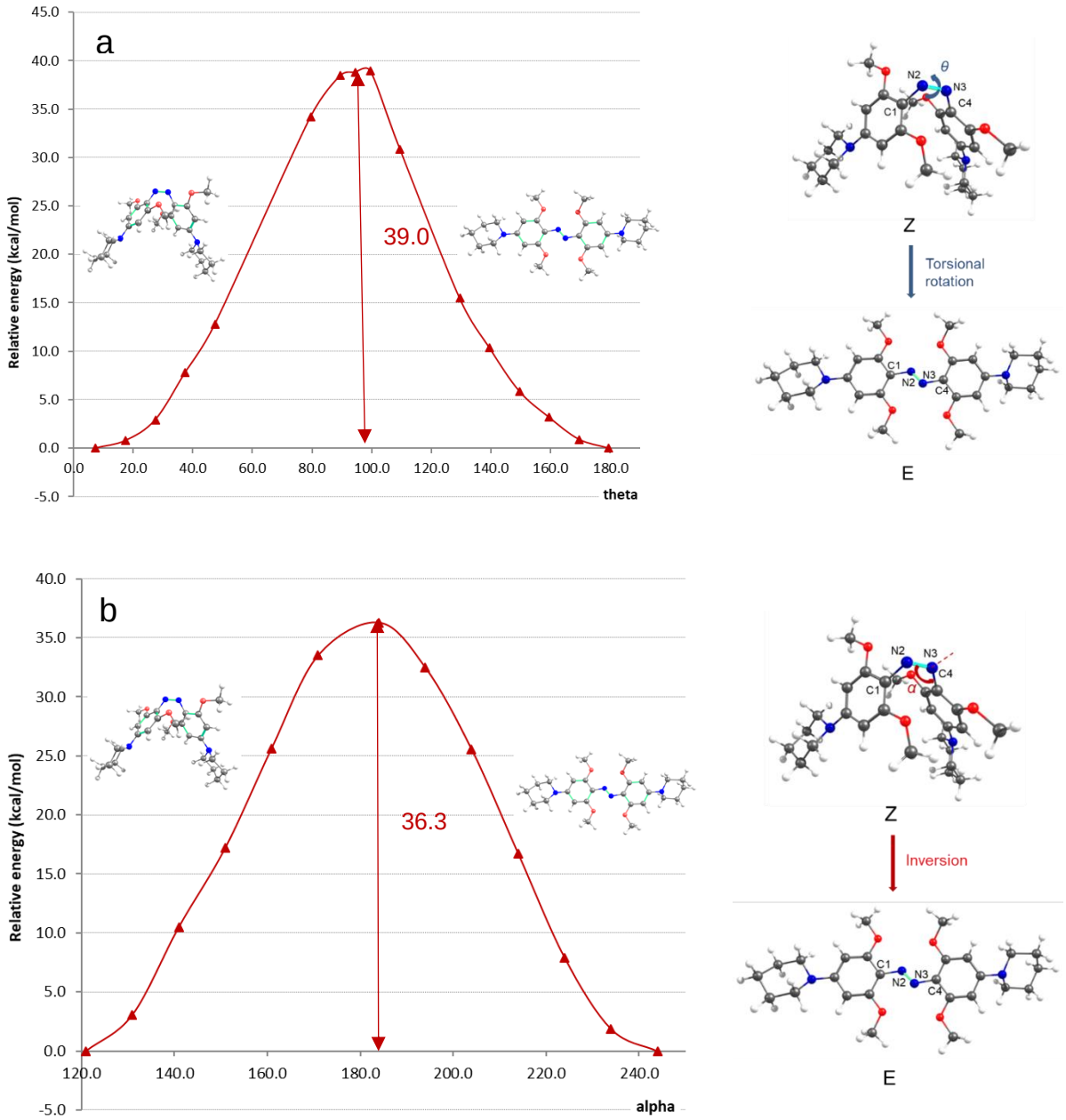

Figure S14.1. Energetics of thermal isomerization (*Z* ↔ *E*).

Relaxed scans for back isomerization of ***E*** to ***Z*** obtained at the M06-2X/ 6-31+G(d)/SMD (water) level of theory. (a) Torsional rotation (dihedral angle θ(C1-N2-N3-C4)), (b) inversion (bond angle α(N2-N3-C4)).

S15. The validity of barriers and the CI structure (SF-TD-DFT results)

Table S15.1. Parameters for the CI of protonated form (*Z*-H$^+$ ↔ *E*-H$^+$)

S^2 values, $S_0 \rightarrow S_1$ vertical excitation energies and relative energies (w.r.t. ***E*-H$^+$**) for reactants, products, transition states (TSs) and the minimum energy conical intersection (MECI) structure (displayed in Figure S15.1) obtained at the SF-TD-BHHLYP/6-31++G(d,p)/SMD(water) level for geometries optimized with M06-2X/6-31+G(d)/SMD (for ***E*-H$^+$**, ***Z*-H$^+$**, and TSs) and SF-TD-BHHLYP/6-31++G(d,p) (*i.e.*, in the gas phase for MECI), respectively.

System	S^2 (S_0 state)	S^2 (S_1 state)	$\Delta E(S_1\text{-}S_0)$ (eV)	$\Delta E(S_1\text{-}S_0)$ (kcal/mol)	$\Delta E(X\text{-}S_0(E\text{-}H^+))$ (kcal/mol)
***E*-H$^+$**	0.08	0.26	2.71	62.5	0.0
***Z*-H$^+$**	0.08	0.55	2.76	63.7	11.3
TS-torsion (H^+)	0.08	0.11	1.09	25.2	37.8
TS-inversion (H^+)	0.09	0.67	2.98	68.7	38.2
CI (H^+)	0.03	0.29	0.00	0.0	42.1[a]

[a] The gas phase value.

Table S15.2. Parameters for the CI of neutral form (*Z* ↔ *E*).

S^2 values, $S_0 \rightarrow S_1$ vertical excitation energies and relative energies (w.r.t. ***E***) for reactants, products, transition states (TSs) and the MECI structure (displayed in Figure S15.1) obtained at the SF-TD-BHHLYP/6-31++G(d,p)/SMD (water) level for geometries optimized with M06-2X/6-31+G(d)/SMD (for ***E***, ***Z***, and TSs) and SF-TD-BHHLYP/6-31++G(d,p) (*i.e.*, in the gas phase for MECI), respectively.

System	S^2 (S_0 state)	S^2 (S_1 state)	$\Delta E(S_1\text{-}S_0)$ (eV)	$\Delta E(S_1\text{-}S_0)$ (kcal/mol)	$\Delta E(X\text{-}S_0(E))$ (kcal/mol)
E	0.06	0.09	2.96	68.2	0.0
Z	0.05	0.14	3.10	71.4	6.9
TS-torsion	0.26	0.23	0.79	18.3	39.1
TS-inversion	0.11	0.20	1.42	32.8	40.2
CI	0.04	0.10	0.00	0.0	40.7[a]

[a] The gas phase value.

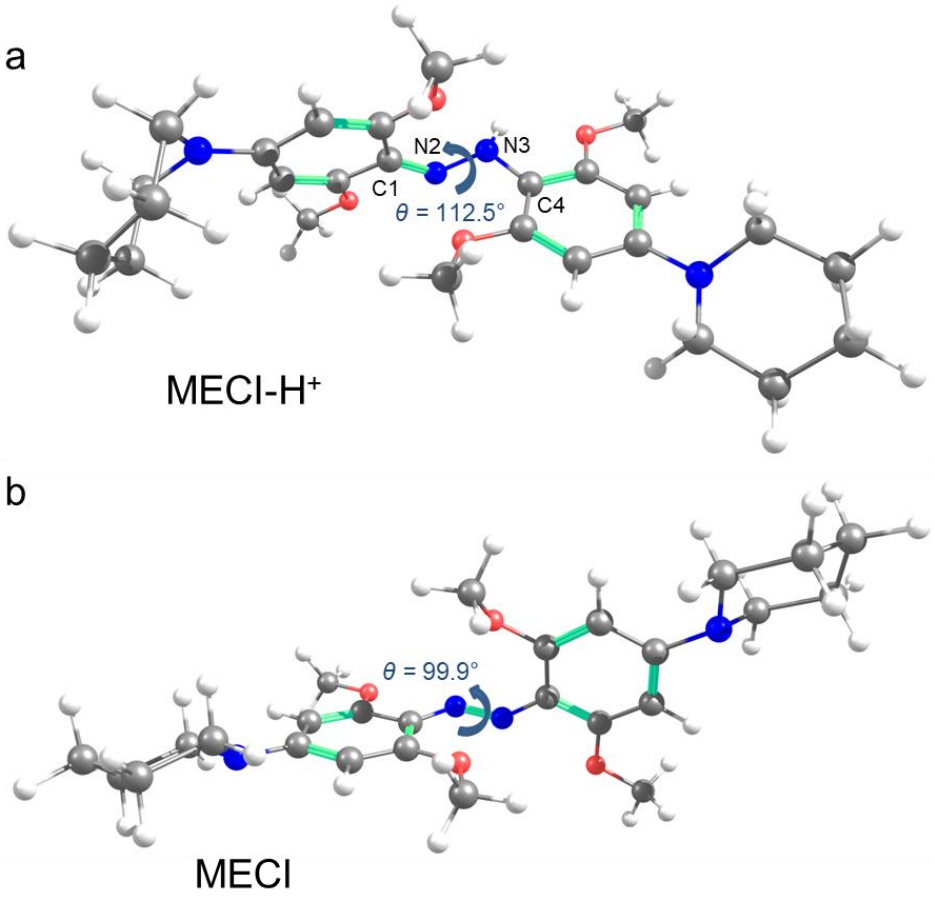

Figure S15.1. Minimum energy conical intersection structures of protonated and neutral forms.

Minimum energy conical intersection (MECI) structures of (a) protonated and (b) neutral forms of **1** obtained at the SF-TD-RO-BHHLYP/6-31++G(d,p) level of theory.

S16. Fitting of transient absorbance data to a kinetic model

Transient absorbance data was collected for pHs 5.9 to 8.75 (Fig. S5.1). However, only for pH ≤ 7.3 were scans fully relaxed in between pulses. The kinetic model used for fitting was:

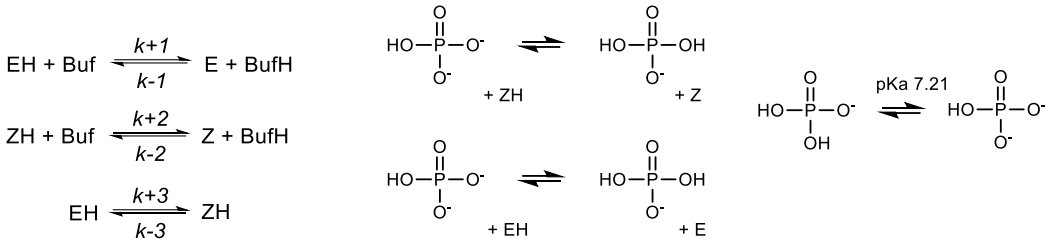

Although the thermal ***E/Z*** isomerization process occurs, it is so slow that it does not contribute to the processes observed in the transient absorbance experiments. Buf and BufH refer to HPO_4^{2-} and $H_2PO_4^-$ respectively. The total phosphate buffer concentration for these experiments was 5 mM (as the potassium salt). The pK_a for the $H_2PO_4^-$/ HPO_4^{2-} + H^+ equilibrium is 7.21. [46] For the pHs used, the buffer concentrations are given in the Table 16.1. In addition, since the pK_a of ***E*-H$^+$** is known (Fig. 1 main text) the equilibrium concentrations of ***E*** and ***E*-H$^+$** can be calculated for each pH. Since both the buffer pK_a and the pK_a of ***E*-H$^+$** are fixed, this sets the ratio (but not the absolute values) of rate constants k+1 and k-1. This ratio was held fixed (k+1/k-1 = 0.323) during global fitting. The degree of protonation was assumed not to change from immediately before to immediately after the pulse.

Table S16.1. Equilibrium values used in Kintek fitting.

pH	[BufH] µM	[Buf] µM	[E] µM	[EH] µM	Absorbance @ 390 nm	Absorbance @ 540 nm
5.9	4766.5	233.5	0.55	34.45	0.229	1.132
6.85	3480.6	1519.4	4.33	30.66	0.261	1.022
7.02	3038.3	1961.7	6.05	28.95	0.276	0.972
7.12	2758.1	2241.9	7.29	27.71	0.287	0.936
7.21	2500	2500	8.55	26.44	0.298	0.899
7.31	2213.4	2786.6	10.13	24.87	0.311	0.853

For each pH condition the equilibrium values of ***E*** and ***E*-H$^+$** were changed at time zero to simulate the nanosecond pulse. A fraction of ***E*-H$^+$** was converted to ***Z*-H$^+$** and a fraction of ***E*** was converted ***Z***. These fractions were systematically varied as part of the fitting process. The pulse energy is high enough that essentially all molecules are expected to be excited. As a result, the fractions converted represent estimates of the quantum yields for isomerization. The observables used for fitting were the absorbance (@540 nm and @390 nm) minus the equilibrium absorbance at each wavelength:

$$\Delta A(540)_{pH} = (0.0328*EH) + (0.00365*E) + (a*ZH) + (b*Z) - Abs@540(eq)_{pH}$$

$$\Delta A(390)_{pH} = (0.0064*EH) + (0.015*E) + (c*ZH) + (d*Z) - Abs@390(eq)_{pH}$$

Measured absorbances were averaged over a 10 nm window. Since only 1 mm of a 10 mm cell is exposed to the ns pulse, absorption coefficients were scaled by a factor of 0.1 to account for

this. Global fitting was then performed using Kintek to find best fit values for rate constants k+1, k-1 (ratio fixed), k+2, k-2, k+3, k-3 as well as the parameters a,b,c, and d (the absorption coefficients for ***Z*** and ***Z*-H**$^{+}$). Fits are shown in Fig. 16.1. Table 16.2 lists best fit values and associated standard errors.

To obtain values for the absorption coefficients for ***Z*** and ***Z*-H**$^{+}$ at other wavelengths, data at pH 6.85 were used and rate constants were held fixed. Transient absorbance data as a function of wavelength were then fitted to find values of a,b,c, and d as a function of wavelength.

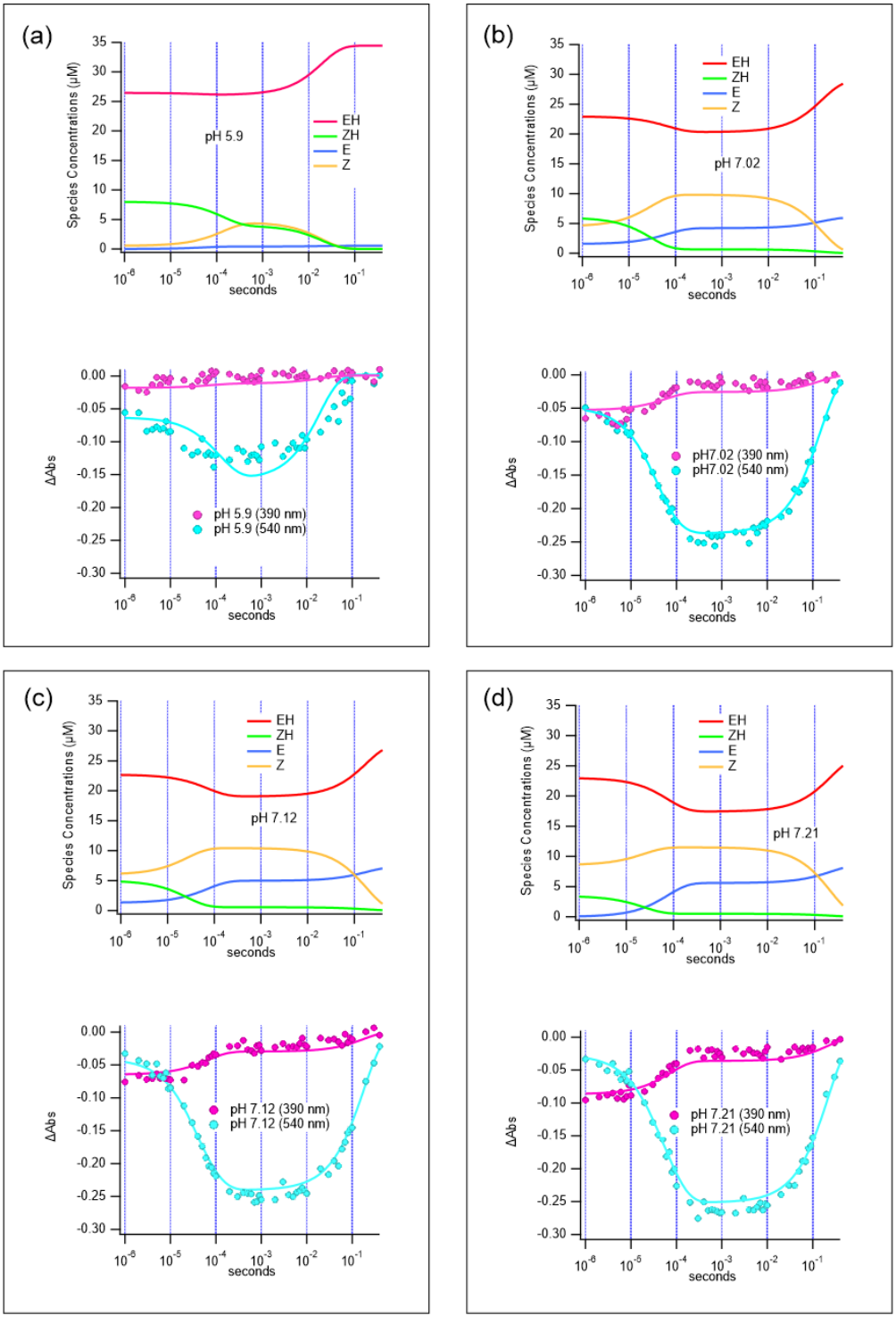

Fig. S16.1. Global fits to nanosecond transient absorbance data at different pHs.

Time resolved absorbance difference measured at 390 nm (magenta) and 540 nm (cyan) and calculated concentrations of ***E*-H$^+$**, ***Z*-H$^+$**, ***E*** and ***Z*** after a nanosecond pulse for the system at pH 5.9 (a), pH 7.02 (b), 7.12, (c), and 7.21 (d). Fits calculated using Kintek Explorer are shown as solid lines.

Table S16.2. Fitted values derived from Kintek.

pH	Fraction ***E*-*H*$^+$** isomerized	Fraction ***E*** isomerized
5.9	0.23 ± 0.07	1 ± 0.07
6.85	0.21 ± 0.07	0.77 ± 0.06
7.02	0.20 ± 0.07	0.74 ± 0.06
7.12	0.18 ± 0.06	0.82 ± 0.07
7.21	0.13 ± 0.05	0.88 ± 0.07
7.31	0.15 ± 0.05	0.90 ± 0.07

Constant	Fitted value
k+1	1.28 ± 0.07 $\mu M^{-1}s^{-1}$
k-1	3.96 ± 0.07 $\mu M^{-1}s^{-1}$
k+2	16 ± 2 $\mu M^{-1}s^{-1}$
k-2	0.68 ± 0.1 $\mu M^{-1}s^{-1}$
pK_a (*Z*-*H*$^+$)*	5.8 ± 0.15
k+3	0 (N.D.)
k-3	112 ± 12 s^{-1}

*calculated from -log((k+2/k-2)(10^-7.21))

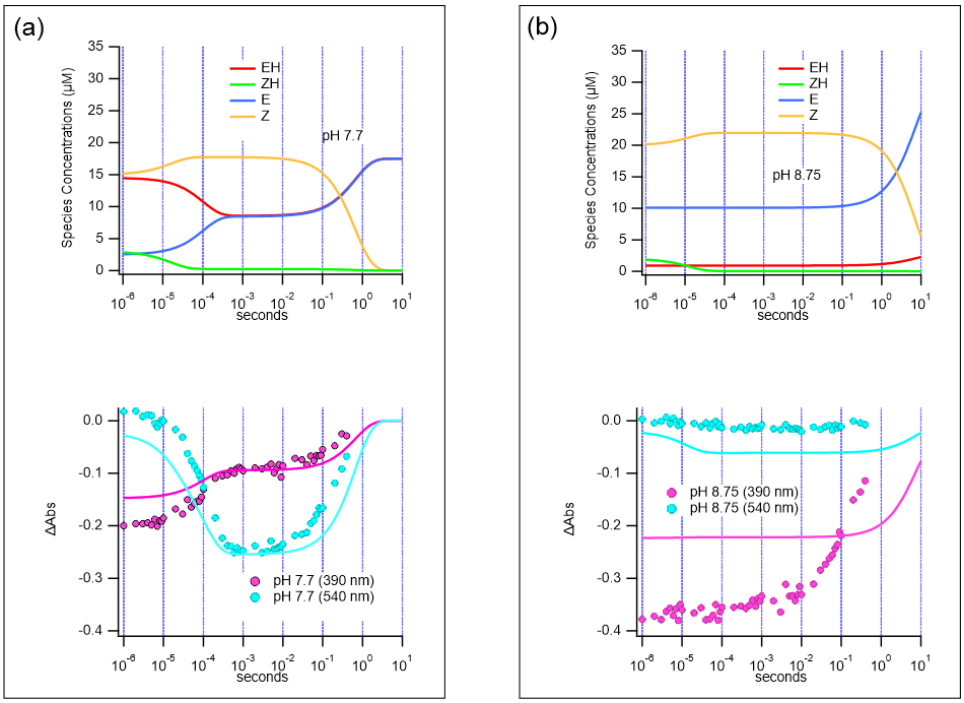

Fig. S16.2. Predicted and observed nanosecond transient absorbance data at high pHs.

Time resolved absorbance difference measured at 390 nm (magenta) and 540 nm (cyan) after a nanosecond pulse for the system at pH 7.7 (a) and pH 8.75 (b). Predicted absorbances and

concentrations of ***E*-H$^+$**, ***Z*-H$^+$**, ***E*** and ***Z*** calculated using Kintek Explorer using parameters from global fitting to pH 5.9 to 7.31 data. Note that the system does not relax completely between pulses under these conditions. As a result, the absorbance difference at 390 nm at the beginning of the measurement is much lower than predicted. Nevertheless, the slowing of the relaxations processes at higher pHs is predicted by the fits.

S17. Estimate of time between absorption events

After photoisomerization from ***E*-H$^+$** to ***Z*-H$^+$**, a single azonium molecule has a lifetime on the order of 10-1000 µs, before dissociating to form ***Z*** and **H$^+$**. If ***Z*-H$^+$** encounters a photon during this period, back photoisomerization to ***E*-H$^+$** is possible. Here we estimate the average time between photon absorption events per molecule as a function of light intensity.

At a concentration of 35 µM in a 1 cm^3 cuvette, the azonium species has an optical density of ~1.0. If this is irradiated with a beam of 650 nm light of intensity **ƶ** (W/cm^2), the number of photons incident on the solution, per second, is:

Number of photons/second: = Intensity **ƶ** (W/cm^2)*Area (cm^2) / Energy per photon (J).
Where Energy (E) per photon = hc / λ. (hc = 1.98644586 × 10^{-25} Jm^{-1}, λ = 650 nm)

= **ƶ** (3.27 × 10^{18}) photons/sec

If OD=1.0, the probability of absorbance in 1 cm path is 0.9.

Thus: 0.9 **ƶ** (3.27 x 10^{18}) photons absorbed/sec

A concentration of 35 µM corresponds to:

35 x 10^{-6} (mol/litre)(6.023 x 10^{23} molecules/mol)/1000 (cm^3/litre) = 2.107 x 10^{16} molecules/cm^3

If the probability of any molecule absorbing a photon is equal the average time between absorption events is:

τ = 2.107 x 10^{16} molecules/cm3 /0.9 **x** (3.27 x 10^{18}) photons absorbed/sec.
For τ = 1000 µs, **ƶ** = 7.15 W/cm^2; for τ = 10 µs, **ƶ** = 715 W/cm^2

Light intensities at the focus of a typical light microscope are ~100 W/cm^2.[47]

S18. References

1. Samanta, S.; Beharry, A. A.; Sadovski, O.; McCormick, T. M.; Babalhavaeji, A.; Tropepe, V.; Woolley, G. A., Photoswitching azo compounds in vivo with red light. *J. Am. Chem. Soc.* **2013,** *135* (26), 9777-84.
2. Samanta, S.; Babalhavaeji, A.; Dong, M. X.; Woolley, G. A., Photoswitching of ortho-substituted azonium ions by red light in whole blood. *Angew. Chem. Int. Ed. Engl.* **2013,** *52* (52), 14127-30.
3. Johnson, K. A.; Simpson, Z. B.; Blom, T., Global kinetic explorer: a new computer program for dynamic simulation and fitting of kinetic data. *Anal. Biochem.* **2009,** *387* (1), 20-9.
4. Fischer, E., Calculation of photostationary states in systems A↔B when only A is known. *J. Phys. Chem.* **1967,** *71* (11), 3704-6.
5. van Stokkum, I. H.; Larsen, D. S.; van Grondelle, R., Global and target analysis of time-resolved spectra. *Biochim. Biophys. Acta.* **2004,** *1657* (2-3), 82-104.
6. Snellenburg, J. J.; Laptenok, S. P.; Seger, R.; Mullen, K. M.; van Stokkum, I. H. M., Glotaran: A Java-based graphical user interface for the R package TIMP. *J. Stat. Softw.* **2012,** *49* (3), 1-22.
7. Henry, E. R., The use of matrix methods in the modeling of spectroscopic data sets. *Biophys. J.* **1997,** *72* (2 Pt 1), 652-73.
8. Zhao, Y.; Truhlar, D. G., The M06 suite of density functionals for main group thermochemistry, thermochemical kinetics, noncovalent interactions, excited states, and transition elements: two new functionals and systematic testing of four M06-class functionals and 12 other functionals. *Theor. Chem. Acc.* **2008,** *120* (1-3), 215-241.
9. Ditchfield, R.; Hehre, W. J.; Pople, J. A., Self-consistent molecular-orbital methods .9. Extended Gaussian-type basis for molecular-orbital studies of organic molecules. *J. Chem. Phys.* **1971,** *54* (2), 724–728.
10. Riplinger, C.; Pinski, P.; Becker, U.; Valeev, E. F.; Neese, F., Sparse maps-A systematic infrastructure for reduced-scaling electronic structure methods. II. Linear scaling domain based pair natural orbital coupled cluster theory. *J. Chem. Phys.* **2016,** *144* (2).
11. Purvis, G. D.; Bartlett, R. J., A Full Coupled-Cluster Singles and Doubles Model - the Inclusion of Disconnected Triples. *J. Chem. Phys.* **1982,** *76* (4), 1910-1918.
12. Raghavachari, K.; Trucks, G. W.; Pople, J. A.; Headgordon, M., A 5th-Order Perturbation Comparison of Electron Correlation Theories. *Chem. Phys. Lett.* **1989,** *157* (6), 479-483.
13. Liakos, D. G.; Sparta, M.; Kesharwani, M. K.; Martin, J. M. L.; Neese, F., Exploring the Accuracy Limits of Local Pair Natural Orbital Coupled-Cluster Theory. *J. Chem. Theor. Comput.* **2015,** *11* (4), 1525-1539.
14. Dunning, T. H., Gaussian-Basis Sets for Use in Correlated Molecular Calculations .1. The Atoms Boron through Neon and Hydrogen. *J. Chem. Phys.* **1989,** *90* (2), 1007-1023.
15. Marenich, A. V.; Cramer, C. J.; Truhlar, D. G., Universal solvation model based on solute electron density and on a continuum model of the solvent defined by the bulk dielectric constant and atomic surface tensions. *J. Phys. Chem. B* **2009,** *113* (18), 6378-6396.
16. Lian, P.; Johnston, R. C.; Parks, J. M.; Smith, J. C., Quantum chemical calculation of p K(a)s of environmentally relevant functional groups: carboxylic acids, amines, and thiols in aqueous solution. *J. Phys. Chem. A* **2018,** *122* (17), 4366-4374.
17. Shao, Y. H.; Head-Gordon, M.; Krylov, A. I., The spin-flip approach within time-dependent density functional theory: Theory and applications to diradicals. *J. Chem. Phys.* **2003,** *118* (11), 4807-4818.
18. Casanova, D.; Krylov, A. I., Spin-flip methods in quantum chemistry. *Phys. Chem. Chem. Phys.* **2020,** *22* (8), 4326-4342.
19. Yanai, T.; Tew, D. P.; Handy, N. C., A new hybrid exchange-correlation functional using the Coulomb-attenuating method (CAM-B3LYP). *Chem. Phys. Lett.* **2004,** *393* (1-3), 51-57.
20. Christiansen, O.; Koch, H.; Jorgensen, P., The 2nd-Order Approximate Coupled-Cluster Singles and Doubles Model CC2. *Chem. Phys. Lett.* **1995,** *243* (5-6), 409-418.

21. Caricato, M.; Mennucci, B.; Tomasi, J.; Ingrosso, F.; Cammi, R.; Corni, S.; Scalmani, G., Formation and relaxation of excited states in solution: A new time dependent polarizable continuum model based on time dependent density functional theory. *J. Chem. Phys.* **2006,** *124* (12), 124520.
22. Guido, C. A.; Chrayteh, A.; Scalmani, G.; Mennucci, B.; Jacquemin, D., Simple protocol for capturing both linear-response and state-specific effects in excited-state calculations with continuum solvation models. *J. Chem. Theory Comput.* **2021,** *17* (8), 5155-5164.
23. Frisch, M. J., G. W. T., H. B. Schlegel, G. E. Scuseria, M. A. Robb, J. R. Cheeseman, G. Scalmani, V. Barone, B. Mennucci, G. A. Petersson, H. Nakatsuji, M. Caricato, X. Li, H. P. Hratchian, A. F. Izmaylov, J. Bloino, G. Zheng, J. L. Sonnenberg, M. Hada, M. Ehara, K. Toyota, R. Fukuda, J. Hasegawa, M. Ishida, T. Nakajima, Y. Honda, O. Kitao, H. Nakai, T. Vreven, J. A. Montgomery, Jr., J. E. Peralta, F. Ogliaro, M. Bearpark, J. J. Heyd, E. Brothers, K. N. Kudin, V. N. Staroverov, R. Kobayashi, J. Normand, K. Raghavachari, A. Rendell, J. C. Burant, S. S. Iyengar, J. Tomasi, M. Cossi, N. Rega, J. M. Millam, M. Klene, J. E. Knox, J. B. Cross, V. Bakken, C. Adamo, J. Jaramillo, R. Gomperts, R. E. Stratmann, O. Yazyev, A. J. Austin, R. Cammi, C. Pomelli, J. W. Ochterski, R. L. Martin, K. Morokuma, V. G. Zakrzewski, G. A. Voth, P. Salvador, J. J. Dannenberg, S. Dapprich, A. D. Daniels, Ö. Farkas, J. B. Foresman, J. V. Ortiz, J. Cioslowski, and D. J. Fox *Gaussian 09, Revision B.01*, Gaussian, Inc.: Wallingford CT, 2009.
24. Frisch, M. J.; Trucks, G. W.; Schlegel, H. B.; Scuseria, G. E.; Robb, M. A.; Cheeseman, J. R.; Scalmani, G.; Barone, V.; Petersson, G. A.; Nakatsuji, H.; Li, X.; Caricato, M.; Marenich, A. V.; Bloino, J.; Janesko, B. G.; Gomperts, R.; Mennucci, B.; Hratchian, H. P.; Ortiz, J. V.; Izmaylov, A. F.; Sonnenberg, J. L.; Williams; Ding, F.; Lipparini, F.; Egidi, F.; Goings, J.; Peng, B.; Petrone, A.; Henderson, T.; Ranasinghe, D.; Zakrzewski, V. G.; Gao, J.; Rega, N.; Zheng, G.; Liang, W.; Hada, M.; Ehara, M.; Toyota, K.; Fukuda, R.; Hasegawa, J.; Ishida, M.; Nakajima, T.; Honda, Y.; Kitao, O.; Nakai, H.; Vreven, T.; Throssell, K.; Montgomery Jr., J. A.; Peralta, J. E.; Ogliaro, F.; Bearpark, M. J.; Heyd, J. J.; Brothers, E. N.; Kudin, K. N.; Staroverov, V. N.; Keith, T. A.; Kobayashi, R.; Normand, J.; Raghavachari, K.; Rendell, A. P.; Burant, J. C.; Iyengar, S. S.; Tomasi, J.; Cossi, M.; Millam, J. M.; Klene, M.; Adamo, C.; Cammi, R.; Ochterski, J. W.; Martin, R. L.; Morokuma, K.; Farkas, O.; Foresman, J. B.; Fox, D. J. *Gaussian 16 Rev. C.01*, Wallingford, CT, 2016.
25. Schmidt, M. W.; Baldridge, K. K.; Boatz, J. A.; Elbert, S. T.; Gordon, M. S.; Jensen, J. H.; Koseki, S.; Matsunaga, N.; Nguyen, K. A.; Su, S. J.; Windus, T. L.; Dupuis, M.; Montgomery, J. A., General atomic and molecular electronic-structure system. *J. Comput. Chem.* **1993,** *14* (11), 1347-1363.
26. Gordon, M. S.; Schmidt, M. W., Advances in electronic structure theory: GAMESS a decade later. In *Theory and Applications of Computational Chemistry: The First Forty Years*, Dykstra, C. E.; Frenking, G.; Kim, K. S.; Scuseria, G. E., Eds. Elsevier: Amsterdam, 2005; pp 1167-1189.
27. TURBOMOLE *TURBOMOLE V7.2: A development of University of Karlsruhe and Forschungszentrum Karlsruhe GmbH, 1989-2007, since 2007 available from: http://www.turbomole.com*, TURBOMOLE GmbH: 2017.
28. Roe, D. R.; Cheatham, T. E., PTRAJ and CPPTRAJ: Software for processing and analysis of molecular dynamics trajectory data. *J. Chem. Theory Comput.* **2013,** *9* (7), 3084-3095.
29. Wang, J. M.; Wang, W.; Kollman, P. A.; Case, D. A., Automatic atom type and bond type perception in molecular mechanical calculations. *J. Mol. Graph. Model.* **2006,** *25* (2), 247-260.
30. Case, D. A.; Babin, V.; Berryman, J. T.; Betz, R. M.; Cai, Q.; Cerutti, D. S.; Cheatham, I., T.E. ; Darden, T. A.; Duke, R. E.; Gohlke, H.; Goetz, A. W.; Gusarov, S.; Homeyer, N.; Janowski, P.; Kaus, J.; Kolossváry, I.; Kovalenko, A.; Lee, T. S.; LeGrand, S.; Luchko, T.; Luo, R.; Madej, B.; Merz, K. M.; Paesani, F.; Roe, D. R.; Roitberg, A.; Sagui, C.; Salomon-Ferrer, R.; Seabra, G.; Simmerling, C. L.; Smith, W.; Swails, J.; Walker, R. C.; Wang, J.; Wolf, R. M.; X., W.; Kollman, P. A. *AMBER 14*, University of California, San Francisco: 2014.
31. Wang, J. M.; Wolf, R. M.; Caldwell, J. W.; Kollman, P. A.; Case, D. A., Development and testing of a general amber force field. *J. Comput. Chem.* **2004,** *25* (9), 1157-1174.
32. Wu, Y. J.; Tepper, H. L.; Voth, G. A., Flexible simple point-charge water model with improved liquid-state properties. *J. Chem. Phys.* **2006,** *124* (2).

33. Breneman, C. M.; Wiberg, K. B., Determining atom-centered monopoles from molecular electrostatic potentials - the need for high sampling density in formamide conformational-analysis. *J. Comput. Chem.* **1990,** *11* (3), 361-373.
34. Seabra, G. D.; Walker, R. C.; Elstner, M.; Case, D. A.; Roitberg, A. E., Implementation of the SCC-DFTB method for hybrid QM/MM simulations within the amber molecular dynamics package. *J. Phys. Chem. A* **2007,** *111* (26), 5655-5664.
35. Walker, R. C.; Crowley, M. F.; Case, D. A., The implementation of a fast and accurate QM/MM potential method in Amber. *J. Comput. Chem.* **2008,** *29* (7), 1019-1031.
36. Gaus, M.; Goez, A.; Elstner, M., Parametrization and benchmark of DFTB3 for organic molecules. *J. Chem. Theory Comput.* **2013,** *9* (1), 338-354.
37. Ryckaert, J.-P.; Ciccotti, G.; Berendsen, H. J. C., Numerical integration of the cartesian equations of motion of a system with constraints: molecular dynamics of n-alkanes. *J. Comput. Phys,* **1977,** *23* (3), 327-341.
38. Olsen, J. M.; Aidas, K.; Kongsted, J., Excited States in Solution through Polarizable Embedding. *J. Chem. Theor. Comp.* **2010,** *6* (12), 3721-3734.
39. Olsen, J. M. H.; Kongsted, J., Chapter 3 - Molecular Properties through Polarizable Embedding. In *Advances in Quantum Chemistry*, Sabin, J. R.; Brändas, E., Eds. Academic Press: 2011; Vol. 61, pp 107-143.
40. Aidas, K.; Angeli, C.; Bak, K. L.; Bakken, V.; Bast, R.; Boman, L.; Christiansen, O.; Cimiraglia, R.; Coriani, S.; Dahle, P.; Dalskov, E. K.; Ekström, U.; Enevoldsen, T.; Eriksen, J. J.; Ettenhuber, P.; Fernández, B.; Ferrighi, L.; Fliegl, H.; Frediani, L.; Hald, K.; Halkier, A.; Hättig, C.; Heiberg, H.; Helgaker, T.; Hennum, A. C.; Hettema, H.; Hjertenæs, E.; Høst, S.; Høyvik, I.-M.; Iozzi, M. F.; Jansík, B.; Jensen, H. J. A.; Jonsson, D.; Jørgensen, P.; Kauczor, J.; Kirpekar, S.; Kjærgaard, T.; Klopper, W.; Knecht, S.; Kobayashi, R.; Koch, H.; Kongsted, J.; Krapp, A.; Kristensen, K.; Ligabue, A.; Lutnæs, O. B.; Melo, J. I.; Mikkelsen, K. V.; Myhre, R. H.; Neiss, C.; Nielsen, C. B.; Norman, P.; Olsen, J.; Olsen, J. M. H.; Osted, A.; Packer, M. J.; Pawlowski, F.; Pedersen, T. B.; Provasi, P. F.; Reine, S.; Rinkevicius, Z.; Ruden, T. A.; Ruud, K.; Rybkin, V. V.; Sałek, P.; Samson, C. C. M.; de Merás, A. S.; Saue, T.; Sauer, S. P. A.; Schimmelpfennig, B.; Sneskov, K.; Steindal, A. H.; Sylvester-Hvid, K. O.; Taylor, P. R.; Teale, A. M.; Tellgren, E. I.; Tew, D. P.; Thorvaldsen, A. J.; Thøgersen, L.; Vahtras, O.; Watson, M. A.; Wilson, D. J. D.; Ziolkowski, M.; Ågren, H., The Dalton quantum chemistry program system. *WIREs Computational Molecular Science* **2014,** *4* (3), 269-284.
41. Reinholdt, P.; Kongsted, J.; Olsen, J. M. H., Polarizable density embedding: A solution to the electron spill-out problem in multiscale modeling. *J. Phys. Chem. Lett.* **2017,** *8* (23), 5949-5958.
42. Gagliardi, L.; Lindh, R.; Karlström, G., Local properties of quantum chemical systems: The LoProp approach. *J. Chem. Phys.* **2004,** *121* (10), 4494-4500.
43. Fdez. Galván, I.; Vacher, M.; Alavi, A.; Angeli, C.; Aquilante, F.; Autschbach, J.; Bao, J. J.; Bokarev, S. I.; Bogdanov, N. A.; Carlson, R. K.; Chibotaru, L. F.; Creutzberg, J.; Dattani, N.; Delcey, M. G.; Dong, S. S.; Dreuw, A.; Freitag, L.; Frutos, L. M.; Gagliardi, L.; Gendron, F.; Giussani, A.; González, L.; Grell, G.; Guo, M.; Hoyer, C. E.; Johansson, M.; Keller, S.; Knecht, S.; Kovačević, G.; Källman, E.; Li Manni, G.; Lundberg, M.; Ma, Y.; Mai, S.; Malhado, J. P.; Malmqvist, P. Å.; Marquetand, P.; Mewes, S. A.; Norell, J.; Olivucci, M.; Oppel, M.; Phung, Q. M.; Pierloot, K.; Plasser, F.; Reiher, M.; Sand, A. M.; Schapiro, I.; Sharma, P.; Stein, C. J.; Sørensen, L. K.; Truhlar, D. G.; Ugandi, M.; Ungur, L.; Valentini, A.; Vancoillie, S.; Veryazov, V.; Weser, O.; Wesołowski, T. A.; Widmark, P.-O.; Wouters, S.; Zech, A.; Zobel, J. P.; Lindh, R., OpenMolcas: From Source Code to Insight. *J. Chem. Theor. Comp.* **2019,** *15* (11), 5925-5964.
44. Beerepoot, M. T. P.; Steindal, A. H.; List, N. H.; Kongsted, J.; Olsen, J. M. H., Averaged solvent embedding potential parameters for multiscale modeling of molecular properties. *J. Chem. Theor. Comp.* **2016,** *12* (4), 1684-1695.
45. Le Bahers, T.; Adamo, C.; Ciofini, I., A qualitative index of spatial extent in charge-transfer excitations. *J. Chem. Theory Comput.* **2011,** *7* (8), 2498-506.
46. Hass, M. A. S.; Hansen, D. F.; Christensen, H. E. M.; Led, J. J.; Kay, L. E., Characterization of conformational exchange of a histidine side chain: Protonation, rotamerization, and tautomerization of His61 in plastocyanin from Anabaena variabilis. *J. Am. Chem. Soc.* **2008,** *130* (26), 8460-8470.

47. Spring, K. R., Fluorescence Microscopy. In *Encyclopedia of Optical and Photonic Engineering*, 2nd ed.; Hoffman, C.; Driggers, R., Eds. CRC Press: Boca Raton, 2016; Vol. 1, pp 755-762.